Modeling Stochastic Scattering Loss due to Random Surface Roughness in Dielectric Waveguides using the Finite-Difference Time-Domain Method

A Thesis
Presented in Partial Fulfillment of the Requirements for the
Degree of Master of Science
with a
Major in Electrical Engineering
in the
College of Graduate Studies
University of Idaho
by
Brian Guiana

Approved by:
Major Professor: Ata Zadehgol, Ph.D.,P.E.
Committee Members: Dennis Sullivan, Ph.D.,P.E.; Ting-Yen Shih, Ph.D.,P.E.
Department Administrator: Joseph Law, Ph.D.,P.E.

December 2023

Abstract

The dielectric slab waveguide (DSW) has been the subject of much analysis in the past decades, with many important applications in high-speed high-bandwidth electromagnetic propagation. Electromagnetic (EM) scattering may be a significant source of degradation in signal and power integrity of high-contrast silicon-on-insulator (SOI) nano-scale interconnects, such as opto-electronic or optical interconnects operating at 100s of THz where two-dimensional (2D) analytical models of DSWs are often used to approximate scattering loss. However, nearly all analysis of the DSW's stochastic propagation loss α (dB/cm), associated with random surface roughness of its sidewalls, has revolved around the transverse-electric (TE) mode of operation. In this work, a formulation is presented to relate the scattering (propagation) loss to the *scattering parameters* (S-parameters) for the smooth waveguide; the results are correlated with results from the finite-difference time-domain (FDTD) method in 2D and 3D space. We propose a normalization factor to the previous 2D analytical formulation for the stochastic scattering loss based on physical parameters of waveguides exhibiting random surface roughness under the exponential autocorrelation function (ACF), and validate the results by comparing against numerical experiments via the 2D FDTD method, through simulation of hundreds of rough waveguides; additionally, results are compared to other 2D analytical and previous 3D experimental results. The FDTD environment is described and validated by comparing results of the smooth waveguide against analytical solutions for wave impedance, propagation constant, and S-parameters. Results show that the FDTD model is in agreement with the analytical solution for the smooth waveguide and is a reasonable approximation of the stochastic scattering loss for the rough waveguide. This work derives analytical expressions for α in the transverse-magnetic (TM) mode, and correlates it against numerical experiments in the method of finite-difference time-domain (FDTD) in both two-dimensional (2D) and three-dimensional (3D) space using duality. We perform several stochastic numerical experiments using FDTD simulation, and show that α correlates well against the proposed 2D analytical model and 2D FDTD in the range of interest.

Acknowledgments

I thank my academic advisor, Ata Zadehgol. His expertise and insight have guided my research from the start. He has had endless patience for me, stayed late at the lab while I edited my code and papers, and showed kindness and support when I needed it most. I thank the members of my committee, Dennis Sullivan and Ting-Yen Shih, without whom I would have never been able to pursue an advanced degree of any kind. I thank the mentors I have found at AMD, Ali Merrick, Tzu-Min Ou, and Emir Mesanovic, who have been instrumental in my introduction to the corporate world. Last, I thank the National Science Foundation and Advanced Micro Devices, Inc. for funding this research.

Dedication

First and foremost, I thank my wife Naomi for her love and support through the late nights and the days spent apart to finish this work. I thank the friends I made along the way, Christine Page and Jon Brett Walters, for reminding me to take a step back when I needed it. I thank Ryan Morgan for being with me since the beginning. Lastly, a well deserved mention to my cats Claire, Eloise, and Phoebe for their warmth and companionship.

Table of Contents

List of Figures

List of Tables

Statement of Contribution

This thesis contains text adapted from multiauthored papers throughout. I was the first author and my major professor and advisor Ata Zadehgol was the second author, and the division of labor was as follows: Writing—original draft, B.G.; Writing—review & editing, A.Z.; Conceptualization, A.Z.; Data curation, B.G.; Formal analysis, B.G. and A.Z.; Funding acquisition, A.Z.; Investigation, B.G. and A.Z.; Methodology, B.G. and A.Z.; Project administration, A.Z.; Resources, A.Z.; Software, B.G.; Supervision, A.Z.; Validation, B.G.; Visualization, B.G.

1 Introduction

Text in this chapter originated from: [1–6, 8, 9].

Nano-scale silicon-on-insulator (SOI) optical interconnects, comprised of silicon/silicon-dioxide (Si/SiO_2) dielectric waveguides operating at 100s of terahertz (THz), constitute an increasingly important building block of modern integrated circuits, where the high-tech market demands smaller form-factors and wavelengths. Considering the non-ideal manufacturing process, random imperfections in the surfaces of nano-scale dielectric waveguides may cause significant signal degradation and power attenuation, as EM waves propagate through the interconnect structure, where the loss is primarily due to EM wave scattering with surface roughness of the waveguide [10–14]. Therefore, the characterization of scattering loss is a topic of significant interest to the scientific community [3, 7, 9–16].

The three-dimensional (3D) structure of SOI optical interconnects poses certain challenges to its analytical and numerical modeling; thus, the stochastic scattering loss observed in nano-scale THz SOI interconnects is often approximated using 2D planar models of the dielectric slab waveguide (DSW) exhibiting surface roughness. The 2D analogue is useful for analytically [7, 14, 16] characterizing the effect of scattering loss on the power attenuation of light waves, and is used as a comparison for both experimental analysis (of physical waveguides) [10–13] and numerical analysis [3, 9–11, 15].

In 1983, Kuznetsov and Haus [17] published their work on using the 3D volume current method (VCM) to evaluate the radiation loss in dielectric waveguide structures. Their work includes analysis of single-line, two-line coupled, and three-line coupled waveguide structures, in the absence of random surface roughness. In 1990, Lacey and Payne [14] released their seminal work analyzing 2D planar waveguides exhibiting random surface roughness for a single-line waveguide structure. Their work applies Green's functions to the structure, operating in the transverse-electric-to-z (TE^z) mode, as an approximation for scattering loss in 3D optical interconnects, and later in 1994 [16] it was updated to use normalized waveguide parameters. In 2005, Barwicz and Haus [15] expanded on both of those developments by applying the 3D VCM to single-line waveguides exhibiting random surface roughness. In each of these cases, despite having relatively simple geometries, the solutions are formulated around complicated integral equations, and the solutions only become more complicated as the geometry becomes more complex, for example by adding roughness, multiple tightly-coupled lines, arbitrary-shaped lines or grating, etc., thus limiting the application of integral-based solutions. An effective workaround to the integral-equation complication is to reformulate the problem around differential-equations, leading to the FDTD method. A version of the FDTD method based on wavelets is used in [11], but the details of the FDTD formulation are not included. The FDTD method is also used in [10] through the software tool *Lumerical*, but again details of the FDTD methodology are absent.

An additional problem being addressed by the present manuscript is the lack of an analytical model for the TM-mode stochastic scattering loss in DSWs exhibiting *exponential* surface roughness on their sidewalls. Such a model is important as it would facilitate expedient propagation-loss analysis due to THz wave scattering in high-speed, high-bandwidth, and realistic dielectric waveguides exhibiting surface roughness, such as optical and opto-electornic interconnects [1, 5, 18].

We derive the analytical expressions for the TM-mode stochastic scattering loss by applying the *duality theorem* to the existing TE-mode loss expressions. In calculating the TM-mode stochastic loss, we evaluate four possible formulation options for normalization of the guided power and select the optimal option based on the effective index. We develop a methodology for the numerical validation of the above derived model, in both 2D and 3D FDTD.

While the FDTD method implemented via a *serial* programming paradigm would be computationally expensive, its highly *parallelizable* nature may provide a potential path to a computationally expedient solution; thus, herein we begin to explore this potential by developing a parallelized implementation of FDTD with a traditional Yee-based algorithm [19, 20] and convolution perfectly matched layer (CPML) [21] boundaries, to characterize the scattering loss in DSWs exhibiting surface roughness.

Interest in the DSW has endured over the past several decades, initially with works such as [14, 16, 17, 22–25], and more recently with works such as [1, 3, 5–7, 9–13, 15, 26–32]. The shift between historical and modern interest in purely dielectric wave-guiding structures may be divided primarily by the release of the seminal work by Lacey and Payne in 1990 [14] detailing a relatively simple model for analytically calculating stochastic scattering loss in DSW structures operating in the optical frequency regime ($\lambda_0 \approx 1.5$ μm) with a followup work in 1994 [16] which simplifies that loss model even further. While the DSW is not necessarily a physically realizable structure, it is the spatially 2D canonical form of SOI waveguide technology, where SOI structures are fully spatially 3D. SOI waveguides with very large dimensions in two directions are often approximated using DSW structures.

The discrepancy between these analytical approaches is further confounded by results from hardware experiments. In 2015, Horikawa, Shimura, and Mogami [12] showed that the Lacey and Payne model overestimates hardware measurements, but they also showed that the VCM model underestimates the same measurements. Further hardware measurements [11, 13, 25, 27, 29, 32] show a variety of measured loss figures, but each shows near correlation with the Lacey and Payne analytical model.

Numerical experiments [10, 11, 26, 30] further show a correlation between hardware experiments and the 2D analytical model. However, in each case there is some discrepancy within the triad of hardware, numerical, and analytical models, where the Lacey and Payne analytical model is typically an overestimation. In [5] it was shown through FDTD simulations that analytical and numerical models may be well-matched through the introduction of a normalization factor in the analytical solution, by formulating input power in terms of physical

waveguide parameters. Previous numerical modeling of stochastic scattering loss includes the VCM method [15], film mode matching [28], and the finite-difference time-domain (FDTD) method [5, 10, 11].

Realistic dielectric waveguides are fully 3D structures. Despite the dimensional discrepancy, 2D analytical models are often used as approximations, provided that there is only tight confinement in one of the two cross-sectional dimensions, where length is functionally infinite along the longitudinal-section in both directions. 3D dielectric waveguides with width much larger than height are spatially inefficient. Therefore, in this paper we conduct numerical experiments in FDTD to determine the limit for width where 2D analytical models may be considered a *good* approximation of 3D dielectric waveguides. The 2D analytical models for wave-impedance Z_w (Ohm) and the propagation-constant β (rad/m) are used for comparison.

The ensuing chapters examine the critical components to stochastic scattering loss due to random surface roughness. Chapter 2 covers the fundamentals behind the two most major components to this research, roughness and scattering loss. The formulation outlines the contribution that results from noise in a physical space and how that translates into power and signal degradation over large distances. Chapter 3 details how the scattering parameters relate to dielectric waveguides, roughness, and scattering loss mechanisms. Chapter 4 explores the effects of scattering loss on a simulated dielectric waveguide, first in the canonical spatially-two-dimensional (2D) form, the DSW, then in the fully realized 3D SOI waveguide. These numerical experiments show the strengths and weaknesses of currently accepted models of scattering loss and highlight some potential improvements to existing formulations.

2 Roughness and Scattering

Text in this chapter originated from: [1–6, 8, 9].

Now, with its history established, there truly is no better way to start exploring the world of roughness than to dive headfirst into it. While the research into scattering loss from roughness dates back decades, and much has been done to make the process more approachable, the subject matter still relies on the reader having knowledge of a broad range of physical phenomena. The formulation provided in this chapter is primarily through an electromagnetic viewpoint. Since the ultimate end for this formulation is simulation and numerical experiment, details are provided in the evaluation methodology for producing simulated roughness capable of interaction with the finite-difference time-domain (FDTD) method for simulation. Since the electromagnetic operation of dielectric waveguides occurs in discrete transverse eigenmodes (modal operation), the formulation covers both transverse electric (TE) and transverse magnetic (TM) modes, and highlights some of the delicate intricacies of the translation between the two. Lastly, we look at the formulation for roughness as a consequence of correlated noise.

2.1 Field Excitation, Modes, and Loss Models

Depending on the field excitation, the DSW may be operated in either the TE^{z} or TM^{z} modes. Similarly, the SOI waveguide may operate in TE^{z}-like or TM^{z}-like modes, but the full 3D fields do not have a readily available analytical form. These modes are time-harmonic in nature, i.e., all time-domain field components may be written as $\hat{F}(t) = \Re\left\{Fe^{\jmath\omega t}\right\}$, where F is a complex phasor, ω (rad/s) is the source angular frequency, $\Re\{x\}$ is the real part of x, and $\jmath = \sqrt{-1}$. The nonzero field components in the TE^{z} mode are E_y, H_x, H_z, and the nonzero field components in the TM^{z} mode are H_y, E_x, E_z [5, 7]. We assume propagation to be along $+\hat{z}$ only.

We may then write the transverse field components along the width, as $E_y(x,z) = \Phi_{\mathrm{TE}}(x)e^{-\jmath\beta z}$ and $H_y(x,z) = \Phi_{\mathrm{TM}}(x)e^{-\jmath\beta z}$, where the phase constant $\beta = n_{\mathrm{eff}}k_0$ (rad/m), k_0 (rad/m) is the free-space wave number, n_{eff} is the effective index for either TE or TM modes as described in [7, Appendix D.C]. The field's spatial distribution is assumed to be in the lowest order mode such that both field amplitudes Φ_{TE} and Φ_{TM} may be characterized by (2.1) [5, 7],

$$\Phi(x) = \begin{cases} A\cos(\kappa x) & |x| \le d \\ A\cos(\kappa d)e^{-\gamma(|x|-d)} & |x| > d \end{cases}, \tag{2.1}$$

where A is peak field amplitude, $\kappa = \sqrt{k_0^2 n_1^2 - \beta^2}$, $\gamma = k_0\sqrt{\beta^2 - k_0^2 n_2^2}$, and each of these components is dependent on the mode of operation [5, 7, 22].

The stochastic propagation loss due to wave scattering with random surface roughness is found by comparing input power to output power using

$$P(z) = P(0)e^{-\alpha z} \quad \text{(W)}. \tag{2.2}$$

and solving for α. However, the per-unit-length ratio between the power radiated from the waveguide and the power guided through it

$$\alpha = \frac{P_{\text{rad}}/2L}{P_g} \qquad (\text{Np/m}), \tag{2.3}$$

is an equivalent formulation to (2.2) but is slightly [14, 16] more mathematically manageable in the limiting case, where α is the scattering propagation loss, $P(0)$ is the input guide power, $P(z)$ is the output guide power a distance of z away from $P(0)$, P_{rad} is the radiated power due to an ensemble average of surface roughness, P_g is the nominal guided power in an unperturbed waveguide, and L is the waveguide length. These were derived for the TE^z mode [5, 7, 14, 16], where both P_{rad} and P_g use only E_y in calculations. P_{rad} in the TE^z mode is expressed as (2.4a) [14, 16]. Then, although the procedure for derivation of α_{TE} may be repeated according to [14] for the TM mode, it is expedient to simply apply the *duality theorem* [23, pp. 311-312] to α_{TE} to obtain the TM mode stochastic loss as (2.4b),

$$\alpha_{\text{TE}} = \frac{P_{\text{rad,TE}}}{2L} = \frac{1}{2}\int_0^{\pi} \frac{1}{\eta_2} \frac{\left\langle |E_y(r,\theta)|^2 \right\rangle}{2L} r d\theta \tag{2.4a}$$

$$\alpha_{\text{TM}} = \frac{P_{\text{rad,TM}}}{2L} = \frac{1}{2}\int_0^{\pi} \eta_2 \frac{\left\langle |H_y(r,\theta)|^2 \right\rangle}{2L} r d\theta, \tag{2.4b}$$

where the $\hat{y}$ field components have been coordinate-transformed from rectangular to polar, $\eta_2 = \sqrt{\mu_0/\epsilon_2}$, $\mu_0 \approx 1.26 \times 10^{-6}$ H/m, and $\langle f(x) \rangle$ is the *ensemble average* [7] of the function $f(x)$ over a rough waveguide of infinite length. The impedance is η_2 since the far-field propagation for P_{rad} is transverse electromagnetic (TEM) and is in the cladding region only. Assuming stochastic propagation loss is ergodic (see [7, Appendix A]) the *spatial average* of surface roughness for a single waveguide of infinite length is equivalent to the ensemble average of an infinite number of rough waveguides with each possessing a finite length.

Using the form of $\left\langle |E_y(r,\theta)|^2 \right\rangle$ presented in [14], the radiated power due to wave scattering off of the surface roughness in the TE^z mode is (2.5a), and application of duality theorem yields the radiated power in the TM^z mode as (2.5b)

$$\frac{P_{\text{rad, TE}}}{2L} = \frac{1}{2\eta_0}\Phi^2_{\text{TE}}(d)(n_1^2 - n_2^2)^2 \frac{k_0^3}{4\pi}\int_0^{\pi} \tilde{R}(\beta - n_2 k_0 \cos(\theta)) d\theta \tag{2.5a}$$

$$\frac{P_{\text{rad, TM}}}{2L} = \frac{\eta_0}{2n_2^2}\Phi^2_{\text{TM}}(d)(n_1^2 - n_2^2)^2 \frac{k_0^3}{4\pi}\int_0^{\pi} \tilde{R}(\beta - n_2 k_0 \cos(\theta)) d\theta, \tag{2.5b}$$

where $R(\zeta)$ is the autocorrelation function (ACF) of the ideal roughness profile, and $\tilde{R}(k)$ is the spatial Fourier transform of $R(\zeta)$ and the *power spectral density* [7] of the roughness.

Any ACF may be used with (2.5). Herein we use the widely referenced *exponential* ACF (2.6) [7, 12–14, 16]

$$R(\zeta) = \sigma^2 e^{-\frac{|\zeta|}{L_c}}, \tag{2.6}$$

where σ (m) is the standard deviation of the probability density function (PDF) of the roughness profile and L_c (m) is the correlation length. The exponential ACF is especially popular as it approximates physical manufacturing processes [13] and the integral of its power spectral density has a closed form analytical solution.

We define the guided power as the power flowing through a DSW in the $+\hat{z}$ direction. Given the field symmetries in (2.1), the guided power may be written as one-sided integrals (2.7a) and (2.7b) where $f^*(x)$ is the complex conjugate of $f(x)$.

$$P_{g,\mathrm{TE}} = \frac{1}{2}\int_{-\infty}^{\infty} \Re\left\{-E_y H_x^*\right\} dx = \int_0^{\infty} \frac{1}{\eta_{g,\mathrm{TE}}} |E_y|^2 dx \tag{2.7a}$$

$$P_{g,\mathrm{TM}} = \frac{1}{2}\int_{-\infty}^{\infty} \Re\left\{E_x H_y^*\right\} dx = \int_0^{\infty} \eta_{g,\mathrm{TM}} |H_y|^2 dx \tag{2.7b}$$

2.1.1 Normalization Factor for TE modes

The core and cladding regions may have a different wave impedance value on the interval $[0, d]$ than on (d, ∞), due to the step index which affects η_g. For the TE^z mode $\eta_{g,\mathrm{TE}} = \frac{\omega\mu_0}{\beta}$ is the best formulation option for modeling scattering loss, i.e., the stochastic FDTD simulation results of Chapter 4 validate this choice [5, 9]. The use of the effective impedance as shown here is derived from (14) and (30) in [5], where the effective impedance was implicitly part of the integration of $\Phi^2(x)$ but has been made explicit here. This leads to the simplified TE^z mode scattering loss equation being [5]

$$\alpha_{\mathrm{TE}} = \frac{1}{N_{\mathrm{F,TE}}} \cos^2\left(\kappa_{\mathrm{TE}} d\right) M_W S_W, \tag{2.8}$$

where related variables are grouped into $M_W = \left(n_1^2 - n_2^2\right)^2 \frac{k_0^3}{4\pi}$, and $S_W = \int_0^{\pi} \tilde{R}(\beta - n_2 k_0 \cos(\theta)) d\theta$. The normalization factor was previously derived [5] as (2.9a), but note that the normalization factor from [14] is equivalent to (2.9b). We may visualize the effect of normalization in P_g through comparison of power density distribution across the height of a smooth DSW. Fig. 2.1a shows the TE^z mode distribution with the [14]- and [5]-type normalization factors (diamonds and squares, respectively), the analytical distribution, and the $E \times H^*$ distribution.

$$N_{\mathrm{F,TE}} = n_{\mathrm{eff,TE}} \left(d + \frac{1}{\gamma_{\mathrm{TE}}}\right) = n_{\mathrm{eff,TE}} d_{\mathrm{eff}} \tag{2.9a}$$

$$N_{\mathrm{F,TE}} = n_1 \left(d + \frac{1}{\gamma_{\mathrm{TE}}}\right) = n_1 d_{\mathrm{eff}}, \tag{2.9b}$$

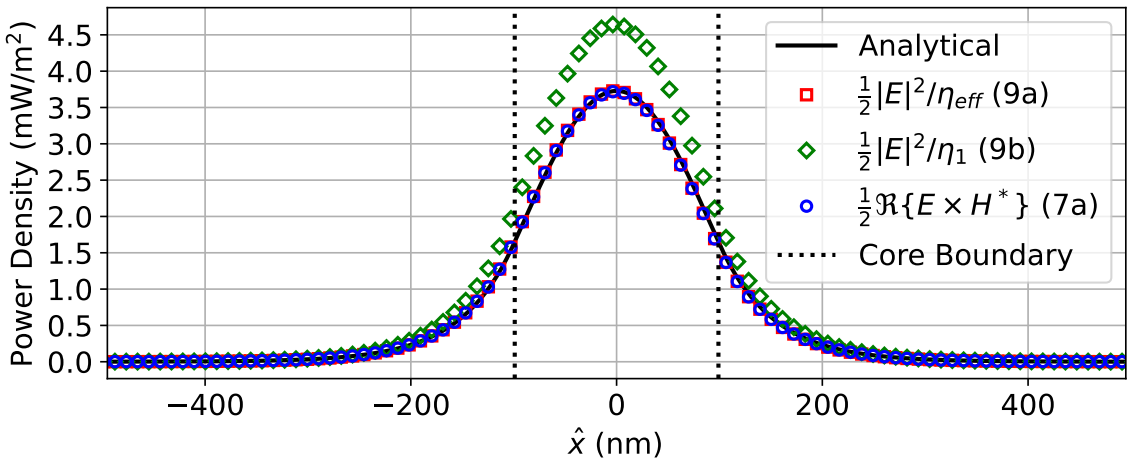

(a)

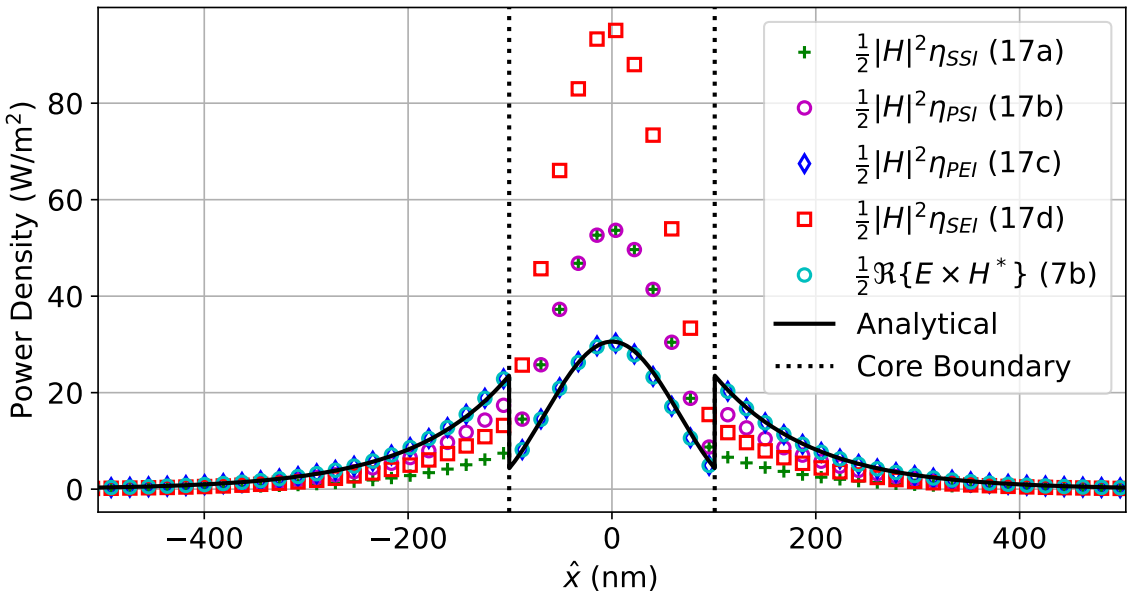

(b)

Figure 2.1: Distribution of power for P_g in the (a) TE^z and (b) TM^z modes for various calculation methods. All discretized fields are computed using 2D FDTD model of a smooth DSW. [1]. This figure was originally published in [2].

where d_{eff} is the effective half-height [7, sec. VI.F], κ_{TE} and γ_{TE} are κ and γ evaluated for the TE mode [7, Appendix D.C]. The distinction between d and d_{eff} is made primarily due to method by which electromagnetic power is transmitted through dielectric waveguides. Much of the power, particularly in the TM-mode, is carried on the surface of the waveguide, and as the height shrinks, the potential power decay grows exponentially. This is illustrated in Fig. 2.2, which depicts the propagation loss as a function of waveguide height in the DSW. α_0 shows the results from Fig. 2 in [13], α_1 is based on β from [23] based on the solution of (2.10), and α_2 is based on β from the *effective index method* [24]. The $1/d^2$ curve is shown as reference for comparing losses.

$$(\mu_0/\mu_d)\,(\beta_{yd}h)\tan(\beta_{yd}h) = \alpha_{y0}h\,(\alpha_{y0}h)^2 + (\beta_{yd}h)^2 = a^2, \tag{2.10}$$

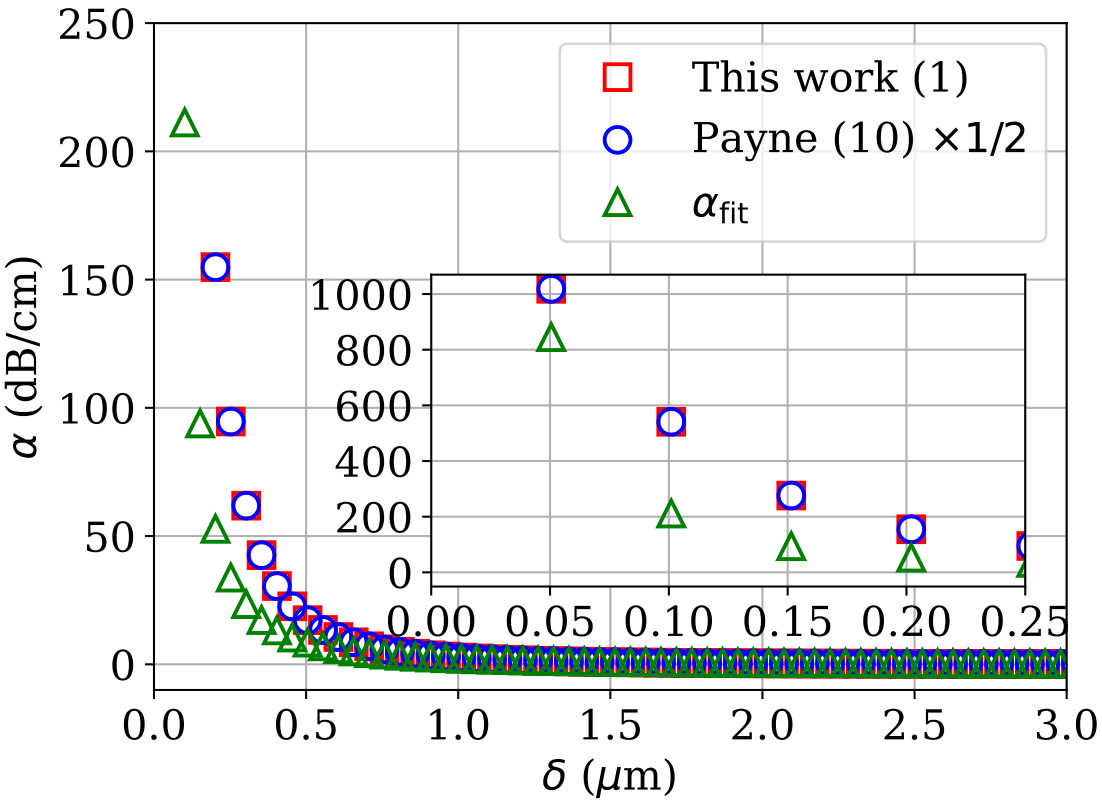

Figure 2.2: Attenuation coefficient α vs. waveguide width. This figure was originally published in [3]. ©2021 USNC-URSI

2.1.2 Normalization Factor for TM modes

There is not yet a well-established value for $\eta_{g,\text{TM}}$, so we explore the four formulation options, below. For the ideal (smooth) waveguide without roughness $P_{g,\text{TM}}$ may be split into integrals

over core and cladding regions which are evaluated using the methods described in [7, Appendix C.D] with the continuity relationship

$$\tan(\kappa_{\mathrm{TM}} d) = \frac{n_1^2}{n_2^2} \frac{\gamma_{\mathrm{TM}}}{\kappa_{\mathrm{TM}}},$$

where κ_{TM} and γ_{TM} are κ and γ evaluated for the TM mode [7, Appendix D.C], yielding

$$P_{g,\mathrm{TM}} = P_{\mathrm{core}} + P_{\mathrm{clad}} = \frac{A_{\mathrm{TM}}^2 \eta_{\mathrm{core}}}{2} (d + f_{\mathrm{core}} + \frac{\eta_{\mathrm{clad}}}{\eta_{\mathrm{core}}} f_{\mathrm{clad}}), \tag{2.11}$$

where the fractions f_{core} and f_{clad} are (2.12a) and (2.12b), respectively, and η_{core} and η_{clad} are the variables of interest for the below options.

$$f_{\mathrm{core}} = \frac{n_1^2 n_2^2 \gamma_{\mathrm{TM}}}{n_1^4 \gamma_{\mathrm{TM}}^2 + n_2^4 \kappa_{\mathrm{TM}}^2} \tag{2.12a}$$

$$f_{\mathrm{clad}} = \frac{2 n_2^4 \kappa_{\mathrm{TM}}^2}{\gamma_{\mathrm{TM}} \left(n_1^4 \gamma_{\mathrm{TM}}^2 + n_2^4 \kappa_{\mathrm{TM}}^2 \right)} \tag{2.12b}$$

- **Single Simple Impedance (SSI)** In [14], the guide impedance was equivalent to setting $\eta_{\mathrm{core}} = \eta_{\mathrm{clad}} = \eta_1$. Doing the same here yields (2.13).

$$P_{g,\mathrm{TM}} = \frac{A_{\mathrm{TM}}^2 \eta_0}{2 n_1} (d + f_{\mathrm{core}} + f_{\mathrm{clad}}) \tag{2.13}$$

- **Piecewise Simple Impedance (PSI)** Assigning the material impedance for each region independently, i.e., $\eta_{\mathrm{core}} = \eta_1$ and $\eta_{\mathrm{clad}} = \eta_2$, yields (2.14).

$$P_{g,\mathrm{TM}} = \frac{A_{\mathrm{TM}}^2 \eta_0}{2 n_1} (d + f_{\mathrm{core}} + \frac{n_1}{n_2} f_{\mathrm{clad}}) \tag{2.14}$$

- **Piecewise Effective Impedance (PEI)** Following the historical formulation for modal field configurations in the TM^{z} mode, as summarized in [7, Appendix C], enforces $\eta_{\mathrm{core}} = \frac{\beta}{\omega \epsilon_1}$ and $\eta_{\mathrm{clad}} = \frac{\beta}{\omega \epsilon_2}$. This yields (2.15).

$$P_{g,\mathrm{TM}} = \frac{A_{\mathrm{TM}}^2 n_{\mathrm{eff,TM}} \eta_0}{2 n_1^2} (d + f_{\mathrm{core}} + \frac{n_1^2}{n_2^2} f_{\mathrm{clad}}) \tag{2.15}$$

- **Single Effective Impedance (SEI)** Considering the duality between TE^{z} and TM^{z} guided powers, assigning $\eta_{\mathrm{core}} = \eta_{\mathrm{clad}} = \frac{\omega \mu_0}{\beta}$ yields (2.16). This assignment follows from the implication that n_{eff} (and therefore β) already includes the geometric relationship between core and cladding.

$$P_{g,\mathrm{TM}} = \frac{A_{\mathrm{TM}}^2 \eta_0}{2 n_{\mathrm{eff}}} (d + f_{\mathrm{core}} + f_{\mathrm{clad}}) \tag{2.16}$$

The scattering loss α may then be simplified to (2.17)

$$\alpha_{\mathrm{TM}} = \frac{1}{N_{\mathrm{F,opt}}} \cos^2(\kappa_{\mathrm{TM}} d) M_W S_W, \tag{2.17}$$

where M_W and S_W are the same as in (2.8), and $N_{\mathrm{F,opt}}$ is the normalization factor based on the four options for guide power listed in (2.18)

$$N_{\mathrm{F,SSI}} = \frac{1}{n_1}\left(d + f_{\mathrm{core}} + f_{\mathrm{clad}}\right) \tag{2.18a}$$

$$N_{\mathrm{F,PSI}} = \frac{1}{n_1}\left(d + f_{\mathrm{core}} + \frac{n_1}{n_2} f_{\mathrm{clad}}\right) \tag{2.18b}$$

$$N_{\mathrm{F,PEI}} = \frac{n_{\mathrm{eff}}}{n_1^2}\left(d + f_{\mathrm{core}} + \frac{n_1^2}{n_2^2} f_{\mathrm{clad}}\right) \tag{2.18c}$$

$$N_{\mathrm{F,SEI}} = \frac{1}{n_{\mathrm{eff}}}\left(d + f_{\mathrm{core}} + f_{\mathrm{clad}}\right) \tag{2.18d}$$

Fig. 2.1b shows TM^z mode distribution with the each of these normalization factors, the analytical distribution, and the Poynting vector distribution.

In Fig. 2.1, we see that for both TE and modes the Poynting vector calculation results in near-perfect overlap with the analytical solution for power distribution across the height of the waveguide, validating the FDTD simulation. In Fig. 2.1a, the normalization factor in (2.9a) also overlaps the analytical distribution, whereas the normalization factor in (2.9b) results in a large overestimation of P_g, which would make α_{TE} *smaller*. In Fig. 2.1b, the PEI option shows a similar overlap with the analytical distribution compared to the TE^z mode, whereas the SEI option seemingly overestimates the guide power by a significant margin. The PEI and analytical options have a large amount of power density on the *surface* of the waveguide.

It should then be expected that TM^z mode propagation will result in much larger power dissipation per-unit-length compared to TE^z mode propagation. The SEI option redistributes the power such that the power contained within the waveguide core region has far greater emphasis than the surface; this concentration toward the center of the waveguide core produces far different analytical model for comparison with simulation results compared to the PEI, SSI, and PSI normalization factor options, as shown by data in Chapter 4.

2.1.3 Derivation of Attenuation and Phase Coefficients from Modal Solutions of Dielectric Slab Waveguides

There are multiple methods for characterizing networks. Two crucial pieces of information to have are the rate of attenuation and the phase shift between two arbitrary points within a network. Here, the attenuation and phase coefficients (α and β, respectively) are calculated for a DSW. The DSW chosen here is assumed to operate in the transverse electric (TE) mode to the z-direction (TE^z). We assume $\frac{\partial}{\partial y} = 0$ and the electric field of the form expressed by

(2.19). Propagation in the waveguide is assumed to be along $\hat{z}$, with field components defined by equations (56)-(61) in [7].

$$E_y(x,z) = E_{y0}\Phi(x)e^{-(\alpha+j\beta)z} \tag{2.19}$$

The ratio of this expression when evaluated at $z = 0$ and at $z = \ell$, where ℓ is the distance between measurement points in (m), results in (2.20), where the modal amplitude function cancels, leaving only the exponential term and the ratio itself.

$$\frac{E_y(x,\ell)}{E_y(x,0)} = \frac{E_{y0}\Phi(x)e^{-(\alpha+j\beta)\ell}}{E_{y0}\Phi(x)} = e^{-(\alpha+j\beta)\ell} \tag{2.20}$$

The complex logarithm, defined in (2.21), is then applied to this ratio, and the real and imaginary components are separated. Each component is simplified, resulting in expressions for α and β, where the units of α are (Np/m) and the units of β are (rad/m).

$$\mathrm{Log}(z) = \ln|z| + j\arg(z) \tag{2.21}$$

$$\alpha = -\frac{1}{\ell}\ln\left|\frac{E_y(x,\ell)}{E_y(x,0)}\right| \tag{2.22a}$$

$$\beta = -\frac{\arg(E_y(x,\ell)) - \arg(E_y(x,0))}{\ell} \tag{2.22b}$$

2.2 Noise to Roughness

Typical noise found nearly everywhere and correlated roughness are tightly linked. Here we examine three uncorrelated noise distributions and one exponentially correlated noise distribution. Each of these are described by their respective *probability density function (PDF)*. The uncorrelated noise images use uniform, exponential, or Gaussian PDFs. The correlated noise images are generated using the exponential PDF and correlation techniques in [33], where the noise images are 2D. Correlation and spectral data for uncorrelated versus correlated noise images are shown in Fig. 2.3.

The correlated noise images are generated automatically with the Pyspeckle package [33]. The control image (with no noise) and examples of noisy images are shown in Fig. 2.4, where values have been normalized to be in $[0, 1]$. We use a 30×30 pixel resolution to display an arbitrary guided mode for the E-field in a typical K-band waveguide. A noisy image is generated for each real and imaginary component of the E-field distribution, and each image is injected to have signal-to-noise ratio of 1. Magnitude plots for each of the noise images are shown in Fig. 2.4. We see therein that while white noise is applied to the field randomly, the correlated noise appears to "warp" the field pattern rather than simply adding random spikes.

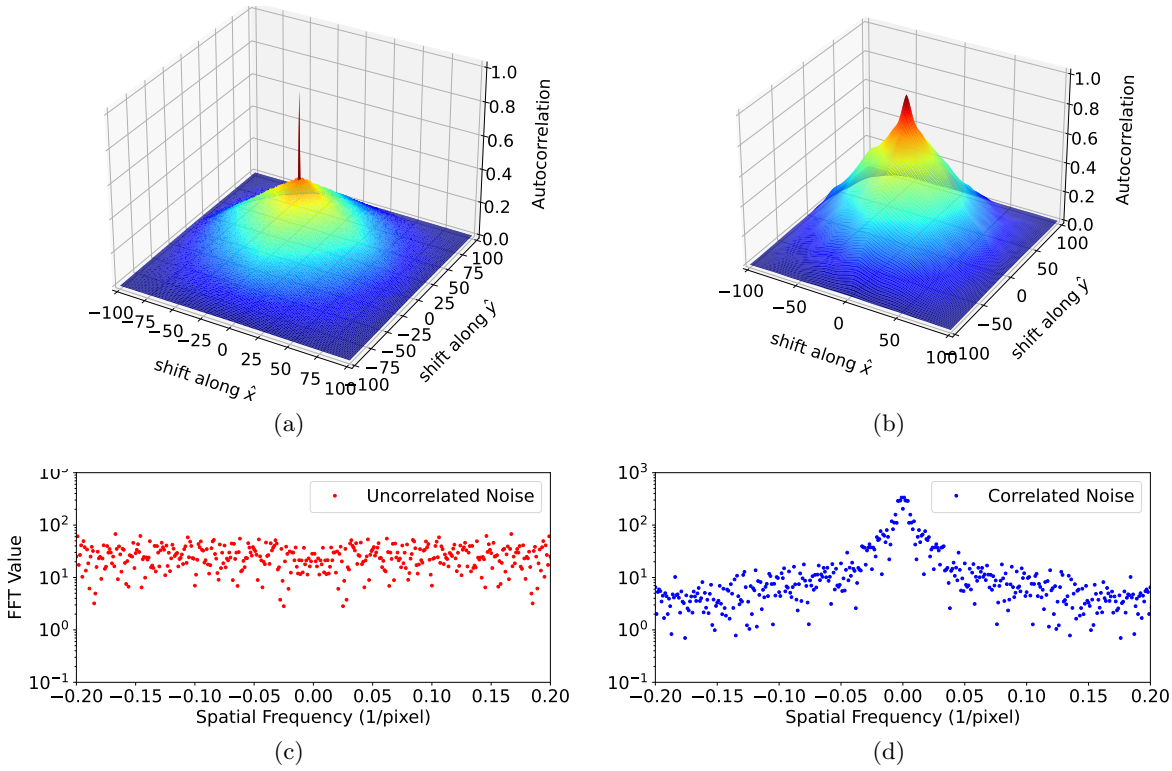

Figure 2.3: (a) Uncorrelated and (b) correlated noise autocorrelation; (c) uncorrelated and (d) correlated noise spectrum. This figure was originally published in [4]. ©2023 USNC-URSI

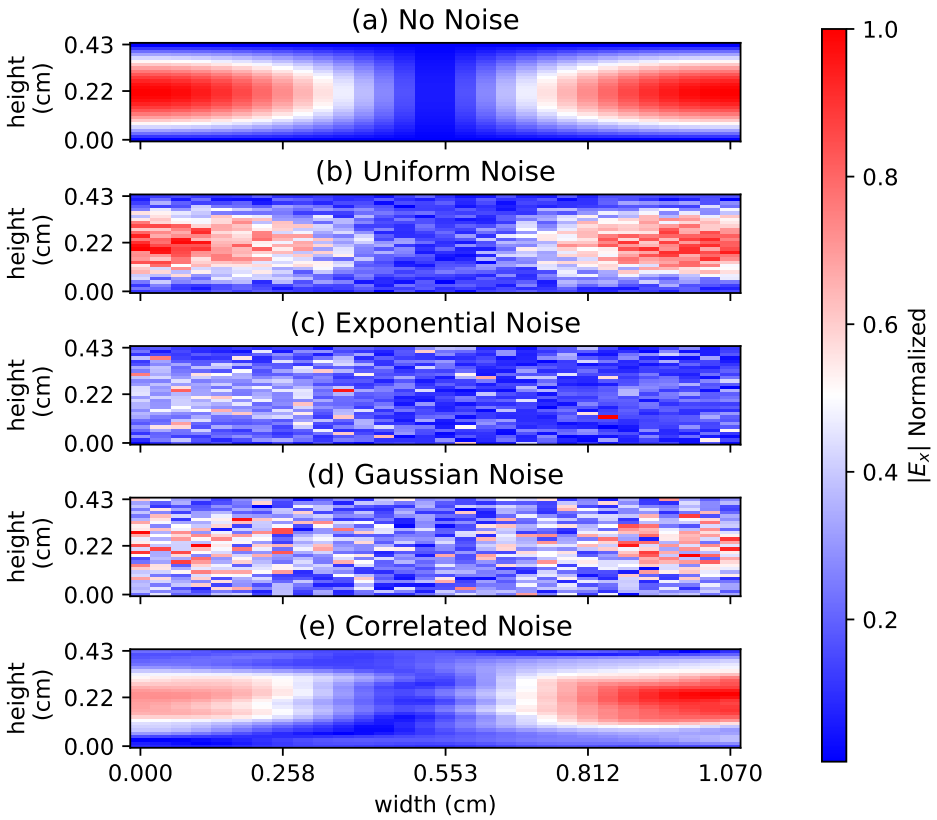

Figure 2.4: Magnitude of E_x in the TE_{11} mode with each noise figure at SNR=1.

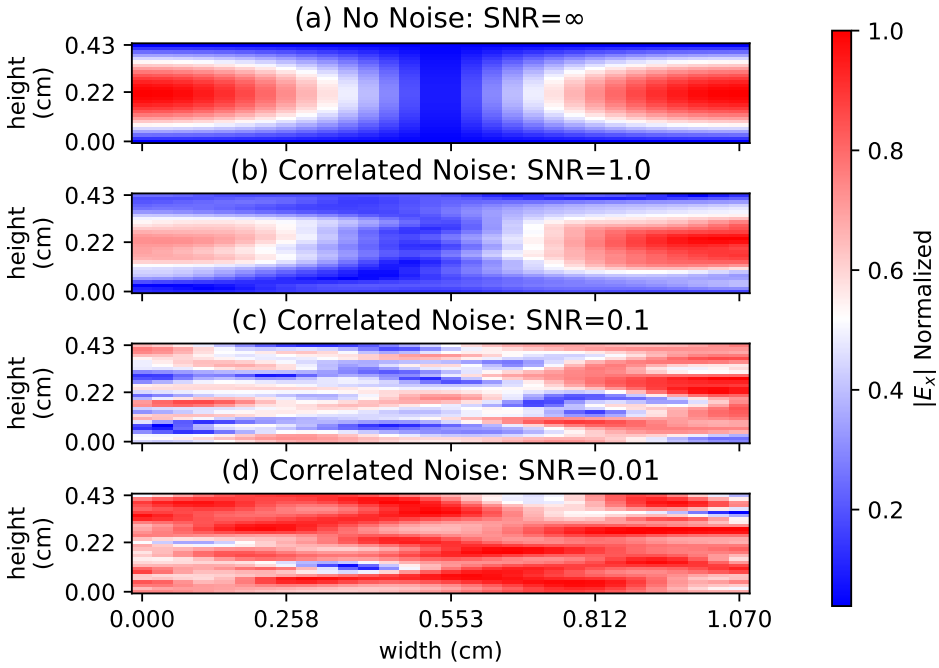

Figure 2.5: Magnitude of E_x in the TE_{11} mode with correlated noise figure at each SNR. This figure was originally published in [4]. ©2023 USNC-URSI

2.3 Verifying the Validity of Discretized Roughness Profiles

In reality, the surface roughness on a dielectric waveguide varies on the atomic scale, such that it is most easily conceptualized as a continuous rough profile. However, both empirical and simulated data requires a sampled profile instead. This causes many issues, some of which may be mitigated through a comprehensive validation methodology. Only through that may a sampled rough profile (as applied to a simulated waveguide) approximate a realistic "continuous" rough surface. The following section outlines the process by which sampled rough profiles are generated and validated prior to their application in FDTD simulation.

We start by assigning a target for σ_{o}, L_{c_o}, and μ_o, where μ designates the *mean* in this subsection. These parameters are then normalized by the spatial discretization step-size Δx value used in the FDTD simulation to yield $\{\sigma = \sigma_o/\Delta x, L_c = L_{c_o}/\Delta x, \mu = 0\}$. The normalized values are passed into the *Pyspeckle* [33] Python library which uses the methods in [34] to generate random profiles; this generation process returns a floating point array of a specified size, whose elements quantify the surface perturbation. A linear offset is added to the aforementioned floating point array to ensure that all values are positive. The offset array is then quantized with the *floor* function and the same linear offset is subtracted from the now integer array, where the final integer array has parameters σ', L_c', and μ'. The error between input (σ) and output (σ') parameters may be quite large, due to the quantization process. However, we may circumvent this issue by constraint-based generation of profiles, described below.

We set a percentage tolerance for the normalized input parameters $\{\sigma, L_c, \mu\}$, and we check that the output parameters $\{\sigma', L_c', \mu'\}$ are within the prescribed tolerance. If a profile does not meet the criteria it is discarded and a new profile is generated. In our numerical experiments, a 10% tolerance is specified by $\sigma' \in [0.9\sigma, 1.1\sigma]$, $L_c' \in [0.9L_c, 1.1L_c]$, and $\mu' \in [-0.01, +0.01]$.

We find σ' and μ' via built-in Numpy functions *std* and *mean*, respectively. We may estimate the L_c' value that fits the autocorrelation data, as explained next. We start by finding the autocorrelation of the generated discretized surface profile using the Pyspeckle *autocorrelate* function which provides a normalized array with its maximum value occurring at $\zeta = 0$. Note the autocorrelation of the generated profile tracks an exponential ACF up to the correlation length, as can be seen in Fig. 2.6. With that in mind, we apply a root finding technique to determine L_c' while using $R_{XX}(L_c') = e^{-1}$ as the reference value. We then subtract e^{-1} from the discrete ACF and find the root closest to $\zeta = 0$, which is the correlation length of the discrete ACF. We may then compare the L_c' with L_c to determine the validity of the generated discretized profile.

For samples with parameter values $\Delta x = 11$ nm and $\sigma = 9$ nm, and knowing that the probability distribution function (PDF) of the random process is *normal* in nature, we know that 99% of values in the final array will be contained in the range $\pm 3\sigma \approx \pm 2.46$. Applying the *floor* function to this range results in the discrete set $\{-3, -2, -1, 0, 1, 2\}$ which may cause significant differences between output values $\{\sigma', L_c', \mu'\}$ and input values $\{\sigma, L_c, \mu\}$.

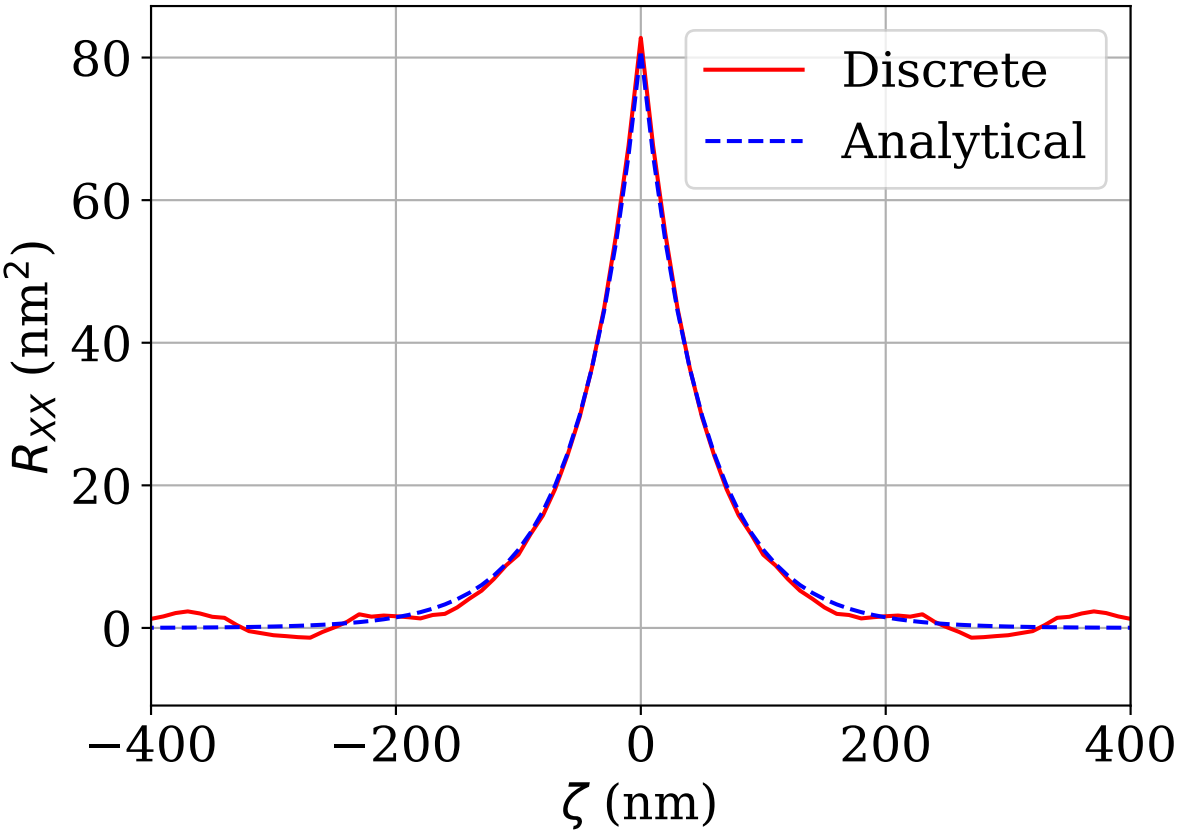

Figure 2.6: Example ACF with input parameters $\sigma = 9$ nm and $L_c = 50$ nm. The discrete trace is generated with 5000 samples. This figure was originally published in [5].

Figure 2.6 compares a discretized exponential ACF comprised of 5000 samples against the continuous analytical ACF (2.6). Even at this small sample size, the discretized profile still correlates well to the ideal ACF up to $\zeta = L_c$, but after that point, there is noticeable noise. At $\zeta = 0$ nm the discretized and continuous analytical ACFs do not line up perfectly. The misalignment at $\zeta = 0$ nm may be remedied by normalizing the analytical ACF to match the discretized ACF, using σ' instead of σ.

3 S-Parameters

Text in this chapter originated from: [1–6, 8, 9].

While it may be convenient to formulate analytical models for scattering loss using the variable physical parameters in a dielectric waveguide, it does not produce such a convenient method for its use in engineering. To that end, this chapter outlines the transition between the more physical approach in the previous chapter toward the usage of the scattering parameters (S-parameters). This approach allows traditional tools, e.g. network analyzers, to be used to acquire empirical data on physical dielectric waveguides which may then be used in conjunction with the previously derived analytical models. The concept is expanded upon through its implementation into the FDTD environment, and a novel formulation for the extraction of S-parameters from the simulated waveguides.

3.1 S-Parameter Computation in a Simulated Environment

S-parameters are often used to characterize a variety of electronic systems [6,9,35]. The methodology of finding S-parameters may be applied to 2D FDTD simulations quite expediently [6, 9]. We use a slight modification of the traditional definition of S-parameters [35], where the total voltage measured at each port in a system can be decomposed into incident and reflected voltages, i.e., $\tilde{V} = \tilde{V}^+ + \tilde{V}^-$, and those components can be used to evaluate S-parameters as in (3.1), where m, n, k are port numbers, $\tilde{V}^+$ is the incident wave, $\tilde{V}^-$ is the reflected wave, and $\tilde{V}$ is the total wave.

$$S_{mn} = \left.\frac{\tilde{V}_m^-}{\tilde{V}_n^+}\right|_{\tilde{V}_k^+=0 \ \forall k \neq n} \tag{3.1}$$

Differing from the traditional definition, instantaneous port power values may be substituted for port voltages, where an additional factor of $1/2$ must be applied to many computations. Electromagnetic power transmission occurs as a power density wave, but an averaging, i.e., surface integration at the port location, must be calculated to reduce the 3D (2+1 spatial/temporal dimensions, respectively) wave to a 1D time-dependent signal per port which may then be converted to a 1D frequency domain signal. In FDTD simulations, we use a two-port system, so $\{m, n, k\} \in \{1, 2\}$. This methodology may be further extended to systems with more ports.

In the simulation grid setup, a variable source is used to excite the fields, and the computational space is divided into the primary domain and the perfectly matched layer (PML) region [21]. The refractive index n is defined as $n = \sqrt{\epsilon/\epsilon_0}$, and the finite dimension of the waveguide is $\delta = 2d$, where d is the half-width or half-height. Electric and magnetic field data are collected over time at ports 1 and 2.

The collection of electric field data for the S-parameters is somewhat complex. An example *baseline* setup and geometry is represented visually in Fig. 3.1, where the waveguide is depicted by the blue region bounded by the solid horizontal black lines, the dashed box is the boundary

between the PML region and the main computational domain, and the red dot is the source location. This source is an infinite line (ILS) due to the 2D field geometry of the example simulation setup. A four-step field evaluation process is required for this single waveguide setup. Parallel waveguides may also be simulated [36], where the number of steps required is equal to the number of ports times two. We are able to record total, incident, and reflected fields in FDTD simulations, but these may not all be recorded simultaneously. The setup for each step of the simulation process for collecting S-parameters is outlined below and shown visually in Fig. 3.2.

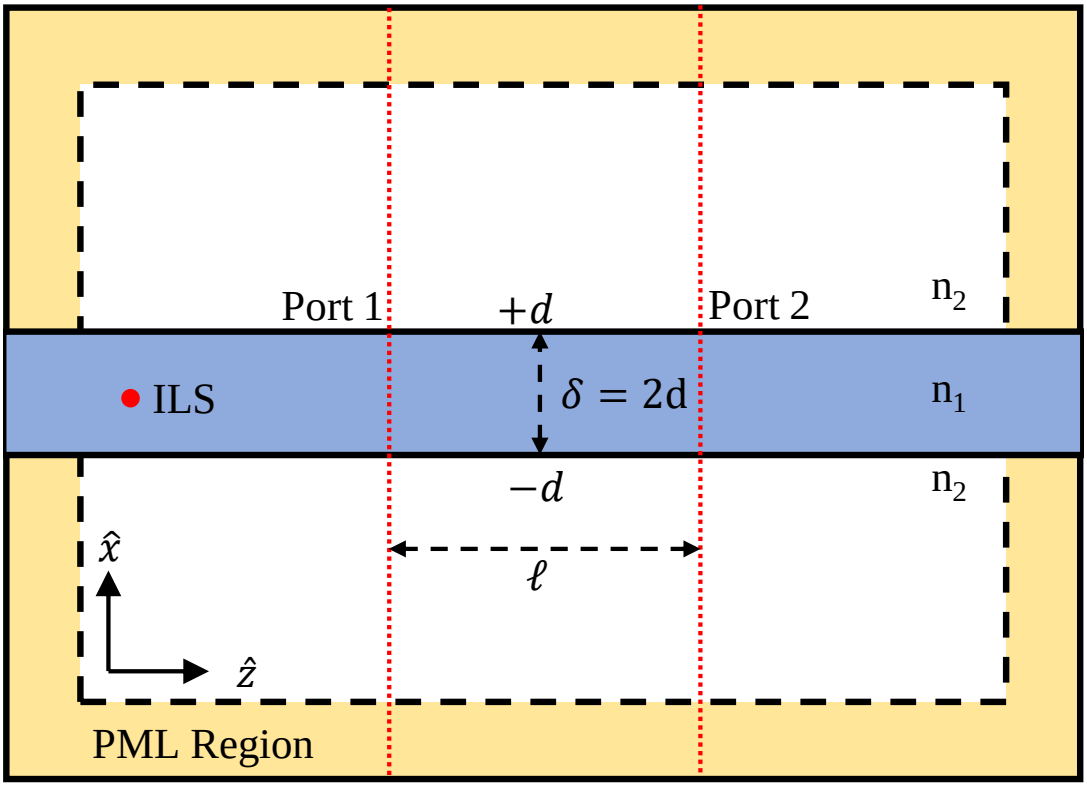

Figure 3.1: FDTD simulation geometry, ILS: Infinite Line Source, $n_1 = 3.5$, $n_2 = 1.5$, Dashed box: primary computational space and the PML region boundary, δ is the width or height of the waveguide, ℓ is the distance between port 1 and port 2, and the dotted red lines are the locations of ports 1 and 2. This figure was originally published in [6]. ©2022 IEEE

Sim 1: The first simulation starts by placing the source condition near port 1, thus enforcing $\tilde{V}_2^+ = 0$ for this simulation. Additionally, we extend the right-side CPML boundary to enclose up to 10 cells to the right of port 1. This simulation records $\tilde{V}_1^+$, so nonideal test parameters, e.g., surface roughness, dispersion, or material variability, are excluded.

Sim 2: The second simulation uses the same source condition as the first. The CPML boundaries are evenly distributed around the computational domain such that fields may interact with any portion of the waveguide. We record $\tilde{V}_1$ and $\tilde{V}_2^-$ during this simulation, and nonideal test parameters are included.

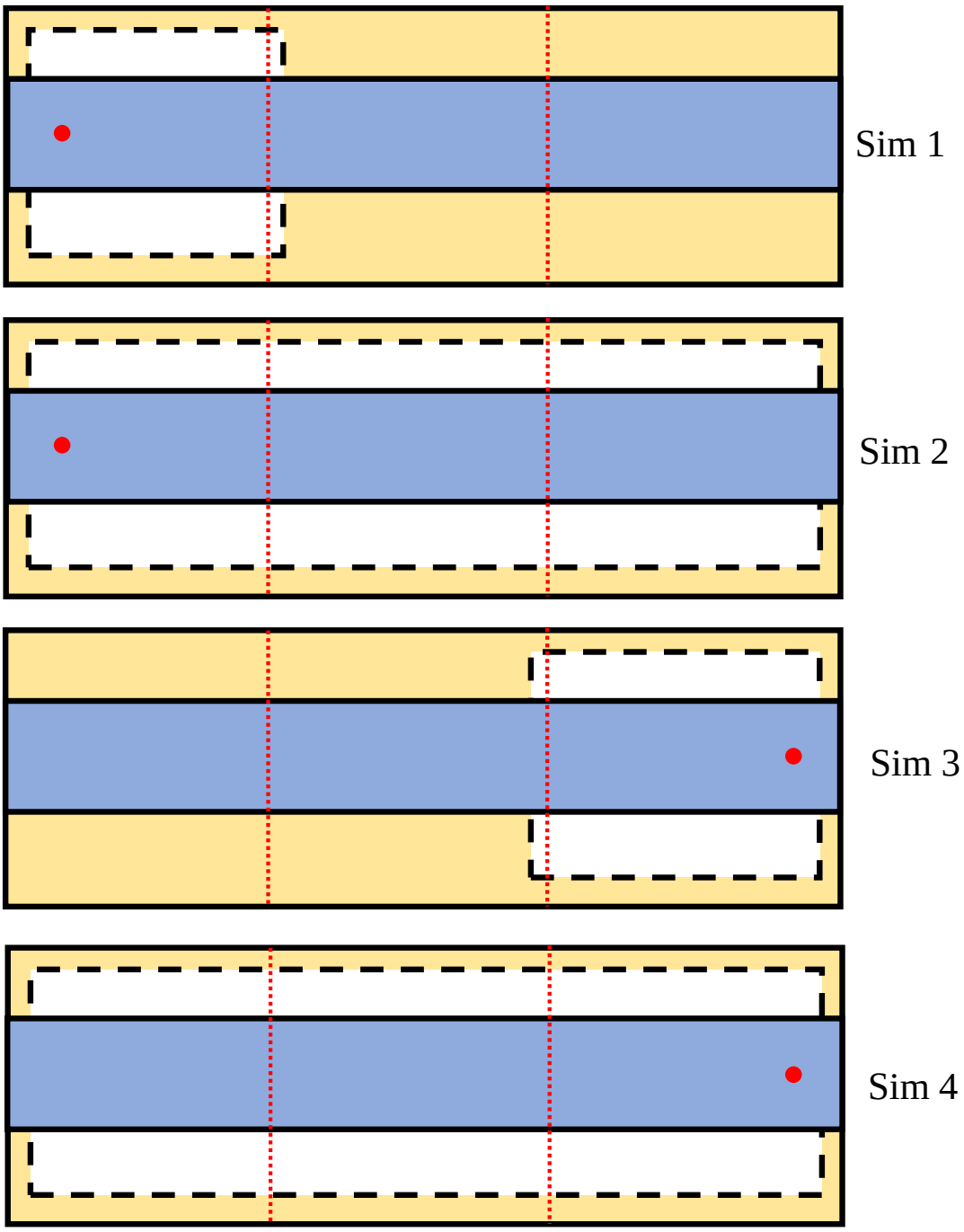

Figure 3.2: S-parameter measurement setup. Field data are collected over time at ports 1 and 2 as defined in Fig. 3.1. The dashed box represents the boundary between the primary computational domain and the PML region. This figure was originally published in [6]. ©2022 IEEE

Sim 3: The third simulation is a mirror of the first. We place the source condition and extend the left-side CPML boundary to be near port 2, thus enforcing $\tilde{V}_1^+ = 0$ in this simulation. Likewise, $\tilde{V}_2^+$ are recorded during this simulation.

Sim 4: The fourth simulation finalizes the port field data collection. It is mirror-like compared to the second simulation. However, nonideal parameters are identical and identically oriented compared to sim 2. Similar to the third simulation, we place the source condition near port 2, with the CPML boundaries matching those in the second simulation. This simulation records $\tilde{V}_1^-$ and $\tilde{V}_2$, concluding the necessary data collection.

The fields directly recorded in the 4-step process are limited to those listed above, but there are still two critically missing field components which are required to fully calculate the scattering matrix. Those being $\tilde{V}_1^-$ where $\tilde{V}_2^+ = 0$, and $\tilde{V}_2^-$ where $\tilde{V}_1^+ = 0$. Here, we may utilize the decomposition relation to find the implicit reflected fields. Specifically, using $\tilde{V}_1^+$ from sim 1 and $\tilde{V}_1$ from sim 2, we may obtain $\tilde{V}_1^- = \tilde{V}_1 - \tilde{V}_1^+$. Similarly, we may recover $\tilde{V}_2^-$ from simulations 3 and 4.

With each of these values calculated from the numerical experiments, the S-parameters matrix may now be computed. In ideal waveguide with no sidewall perturbations, we would expect the S-parameters matrix (of the waveguide system) to be both *symmetric* (*reciprocal*) and *unitary* (lossless) [35]. For a waveguide with sidewall perturbations, we expect the S-parameters matrix (of the waveguide system) to be symmetric (reciprocal) but non-unitary (lossy) [35]. Higher port numbers may be simulated by following the same process of incident field simulation followed by total field simulation, for each port subsequently.

3.2 Computing Power Decay of a 2-port network, Using S-Parameters

The attenuation coefficient in a 2-port network, such as the DSW modeled in Fig. 3.1, can be calculated using the S-Parameters. Starting with **Sim 2**, we take the *total* voltage wave values at both ports 1 and 2, labeling them $\tilde{V}(0)$ and $\tilde{V}(\ell)$, respectively. We assume the voltage waves to have the same form as the electric field where the modal field component $\Phi(x)$ is replaced with an initial voltage V_0, such that $\tilde{V}(z) = V_0 e^{-(\alpha+\jmath\beta)z}$. In this form, it is expected that as z increases, the reference voltage peak will attenuate and its phase will accumulate. With voltage recorded at two port locations, we may begin to determine the complex valued $\alpha + \jmath\beta$ directly. This is done by dividing $\tilde{V}(\ell)$ by $\tilde{V}(0)$, resulting in (3.2).

$$\frac{\tilde{V}(\ell)}{\tilde{V}(0)} = \frac{V_0 e^{-(\alpha+\jmath\beta)\ell}}{V_0} = e^{-(\alpha+\jmath\beta)\ell} \tag{3.2}$$

Using (3.2), α can be isolated through the complex logarithm, (3.3), where $z \in \mathbb{C}$. $\ln(|z|)$ is the natural logarithm (of base e), and arg() is the *total accumulated phase* of z; i.e., the angle of z in relation to the real axis in the complex plane plus any full turns about the origin and may be greater than 2π [37]. For a forward traveling wave, i.e., a wave where power is transferred from port 1 to port 2, we assume that the phase accumulation is always positive.

Applying (3.3) to (3.2) results in (3.4). Equation (3.4) may be separated into real and imaginary components, resulting in the final expression in (3.5), for calculating power loss directly from FDTD experiments.

$$\log(z) = \ln(|z|) + \jmath \arg(z), \tag{3.3}$$

$$-\alpha\ell - \jmath\beta\ell = \ln\left(\left|\frac{\tilde{V}(\ell)}{\tilde{V}(0)}\right|\right) + \jmath \arg\left(\frac{\tilde{V}(\ell)}{\tilde{V}(0)}\right) \tag{3.4}$$

$$\alpha = -\frac{1}{\ell}\ln\left(\left|\frac{\tilde{V}(\ell)}{\tilde{V}(0)}\right|\right) \quad \text{(Np/m)} \tag{3.5}$$

Equation (3.5) is labeled the *direct method* for calculating power loss from FDTD simulation, but there is an alternative definition using incident and reflected fields found through the use of S-Parameters and the corresponding simulations. We start by squaring the input to (3.5), where the labels are reverted from 0 and ℓ to voltages in reference to ports 1 and 2, leading to

$$A = \left|\frac{\tilde{V}(\ell)}{\tilde{V}(0)}\right|^2 = \left|\frac{\tilde{V}_2}{\tilde{V}_1}\right|^2 = \left|\frac{\tilde{V}_2^+ + \tilde{V}_2^-}{\tilde{V}_1^+ + \tilde{V}_1^-}\right|^2 = \frac{\left(\tilde{V}_2^+ + \tilde{V}_2^-\right)\left(\tilde{V}_2^+ + \tilde{V}_2^-\right)^*}{\left(\tilde{V}_1^+ + \tilde{V}_1^-\right)\left(\tilde{V}_1^+ + \tilde{V}_1^-\right)^*}. \tag{3.6}$$

The magnitude-squared operation can be replaced with the equivalent complex operation, resulting in (3.6) where * denotes the complex conjugate operator. This equation for A is reinserted into (3.5) logarithm to recover the expression for α as a function of S-parameters, (3.7) [6], labeled the *S-parameter method*.

$$\alpha = -\frac{1}{\ell}\ln\left(\left|\frac{(1+S_{11})(S_{12})}{S_{11}+S_{12}S_{21}}\right|\right) \quad \text{(Np/m)}. \tag{3.7}$$

Equation (3.7) may also be utilized to obtain values for additional parameters, such as cross-talk, in larger systems by substituting 1 and 2 for some m and n value, respectively.

4 FDTD Analysis Numerical Experiments

Text in this chapter originated from: [1–6, 8, 9].

The previous chapters outlined the fundamental formulation required to analyze dielectric waveguides with random surface roughness. Each component is necessary to understanding the complete picture of the following stochastic experiments. The final piece to the formulation is the actual construction of the FDTD environment which is covered throughout this chapter. The major components to this chapter cover the various numerical experiments that were conducted to verify, highlight, and expand upon previous research in the area of dielectric waveguides, roughness, and power decay from scattering loss. The chapter is divided into two major sections. Section 4.1 details the experiments conducted using the 2D FDTD environment. This includes FDTD setup, environment verification, and stochastic analysis. Section 4.2 details the numerical experiments conducted using the fully 3D FDTD environment. Since the environment is different from 2D FDTD, this is also verified. We examine some aspects unique to 3D waveguides resulting from finite width, and discuss the results from further stochastic analysis. Additionally, information is provided regarding the actual computer implementation of the FDTD environments and some advancements possible with hardware acceleration.

4.1 2D FDTD Numerical Experiments: Results and Discussion

4.1.1 SOI Waveguide with Surface Roughness

We orient the SOI waveguide in space as shown in Fig. 4.1a. The width-height cross-section is centered at the origin, where the height is along $\hat{x}$ and the width is along $\hat{y}$. We assume propagation along the length in the $+\hat{z}$ direction, where the length would ideally extend toward infinity. The highlighted center cut in Fig. 4.1a is shown in Fig. 4.1b. The 2D cross-section additionally serves as the geometry for the corresponding DSW to the SOI waveguide. Typically, if the width of the SOI waveguide is much larger than the height and the variations along width are very small, then the DSW is an appropriate approximation. As width approaches infinity and variations along width approach zero, the SOI waveguide approaches the DSW. An example of surface roughness is shown in Fig. 4.1b alongside the nominal geometry. The example roughness is omitted in Fig. 4.1a but is present on the upper and lower walls of the SOI waveguide and varies only as a function of length, i.e., we assume height perturbations do not vary along width.

We examine the SOI waveguide and DSW composed of two dielectric media, where both are defined by their respective refractive index. Medium 1 (core region) has a refractive index $n_1 = 3.5$ and exists in the SOI waveguide in $-w/2 \leq y \leq +w/2$ and $-d \leq x \leq +d$. The core region has a finite nominal height $\delta = 2d$, where d is the half-height. Medium 2 (cladding region) has refractive index $n_2 = 1.5$ and exists everywhere outside the core region. The refractive index is defined as $n_m = \sqrt{\epsilon_m/\epsilon_0}$, where m is either 1 or 2 and $\epsilon_0 \approx 8.85 \times 10^{-12}$ F/m [3,5–7,9,14,16].

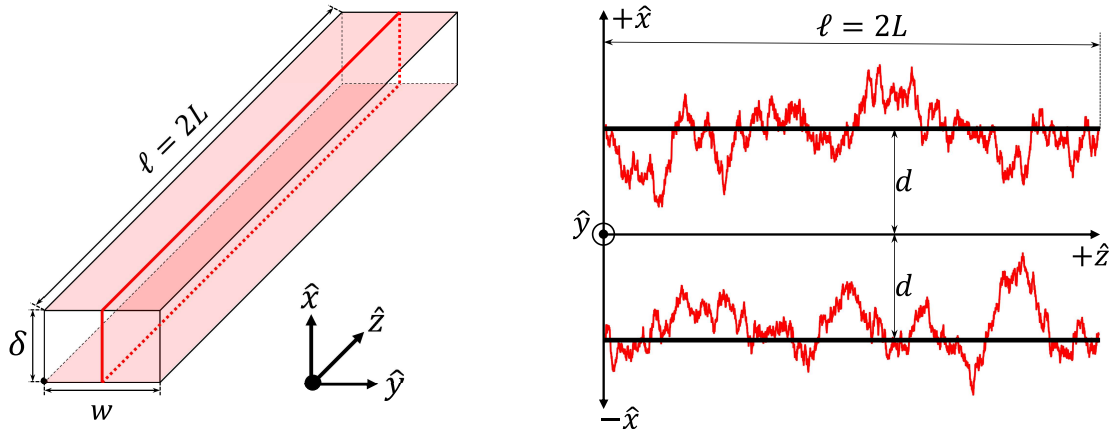

(a) (b)

Figure 4.1: Structural geometry and orientation for the DSW, (a) 3D view, (b) 2D cross-section with roughness example. This figure was originally published in [2].

In 3D space w is finite, but in 2D space w approaches infinity and we may also assume that $\frac{\partial}{\partial_y} \to 0$ for all 2D analysis with this geometry. The waveguides in question exhibit stochastic surface roughness, i.e., random perturbations in height as a function of length. Herein we consider surface roughness with an *exponential* autocorrelation function.

4.1.2 The FDTD Environment

The DSW structure may expediently fit into 2D FDTD analysis. We start by converting the nominal structure into uniform discrete cells with side length Δx. The temporal resolution is then set at the *Courant stability limit* [38] for 2D FDTD, where the background material is set to the cladding medium. We apply the CPML [21] to the exterior of the computational domain, thereby simulating infinite space with minimal reflections and computational cost.

We define length over which we generate and discretize a random profile as ℓ; the remaining cells along the length of the waveguide are buffer space to allow for the source condition to settle into a guided mode (mode settling), before arriving at port 1. Much of the formulation outlined in Chapter 2 uses $2L$ to define the length of the waveguide, but we use ℓ in the FDTD space instead. These are functionally equivalent parameters, and may be used interchangeably.

Once the rough surface profile is ready, it is applied as the core and cladding boundary between ports. Referring to Fig. 4.2, we place a source condition along $\hat{x}$ in a vertical line of cells across the entire mouth of the waveguide, where the distance between the source and CPML is sufficient to disallow interaction between the two. A separation of 10 cells is adequate in most experiments, noting experiments where a different value is required. While we may approximate infinite space with the CPML, we still need to retain a buffer space in the cladding region between the waveguide and CPML boundary as the fields extend beyond the height of the waveguide. To capture the interactions of the EM fields in both the core and cladding regions,

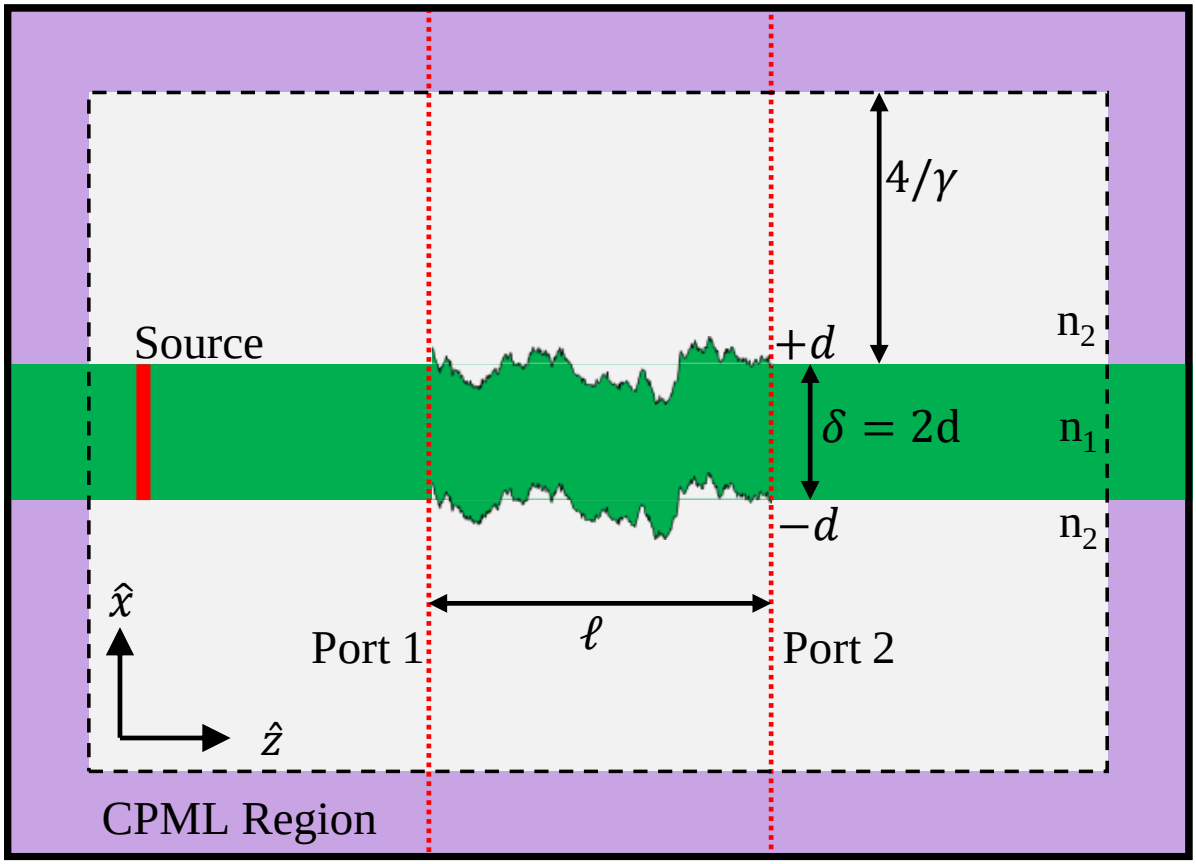

Figure 4.2: The baseline DSW structure. This figure was originally published in [5].

the cladding is size appropriately. In Fig. 2.1 the power wave magnitude decays exponentially in the cladding region with a rate of $1/\gamma$ proportional to distance from the waveguide surface, and that behavior is used to set the buffer size. At a distance of $4/\gamma$ from the waveguide surface, the field magnitude is no more than 2% of its magnitude on the waveguide surface, which is adequate for limiting the interaction between guided waves and the CPML. Electric field data are collected at ports 1 and 2 along the first line of cells adjacent to the rough region. These points are recorded at each time-step over the entire simulation duration. In post-processing, we convert the time-domain E-field values to the frequency domain with the fast Fourier transform (FFT) [39]. We then numerically integrate the E-field over the recorded line of cells, resulting in a frequency dependent voltage with which further analysis may be performed.

We set up the FDTD grid based on the waveguide geometry, material parameters, and desired frequency range. The geometry is set up as shown in Fig. 4.2, where $n_1 = 3.5$ and $n_2 = 1.5$. We set the fundamental frequency as $f_0 = 194.8$ THz (corresponding to source wavelength $\lambda_s = 1.54$ μm). Using the core refractive index, we find the minimum phase velocity $v_{\min}$ (m/s). Using the fundamental frequency, we assign our desired maximum frequency as $f_{\max} = N_H f_0$ (Hz), where N_H is the number of desired harmonics above the fundamental. Using both the minimum phase velocity and the maximum frequency, we find the minimum wavelength simulated in the FDTD scheme with $\lambda_{\min} = v_{\min}/f_{\max}$. Then, our spatial discretization is $\Delta x = \lambda_{\min}/30$ in most experiments, and we note the experiments where that value may differ. We set the time-step Δt at the Courant limit based on the cladding material which has the largest possible phase velocity in the FDTD environment, such that $\Delta t = \frac{\Delta x}{\sqrt{2} v_{\text{clad}}}$.

Testing this setup at $N_H = 2$, $\Delta x \approx 7.3$ nm/cell and the total grid is 5554 cells $\times$ 247 cells ($\hat{z} \times \hat{x}$) with 26,997 time-steps, including 40 layers of CPML as the absorbing boundary condition. Along $\hat{x}$, the core region is centered and the nominal full width measures 36 cells, where the remaining 300 cells are evenly distributed on either side of the core as cladding. Along $\hat{z}$, $\ell = 4092$ cells, and the remaining 1858 cells are evenly distributed to each port region. The computations are done by using a workstation with two Intel® Xeon® E5-2687W v3 CPUs (40 logical cores), operating at 3.10 GHz. Each simulation occupies less than 410 MB of RAM and is completed in roughly 300 seconds.

4.1.3 Modal Transformations and Coordinate Mapping

The geometry used for the characterization of scattering loss from random surface perturbations, shown in Fig. 4.2, is based on the geometry from Fig. 5 in [7]. The fields in [7] are described as TE^{z}, since $E_z = 0$ and $\frac{\partial}{\partial_y} = \partial_y = 0$, and by using (56), (59), and (60) in [7] we know the non-zero field components are $\{E_y, H_x, H_z\}$, while $E_z = E_x = H_y = 0$. The TE^{z} field configuration may also be obtained from (6-72) in [23] and setting $\partial_y = 0$. This is a degenerate configuration as setting $\partial_y = 0$ in (6-64) in [23] yields the TM^{y}, and in (6-74) in [23] yields TE^{x}.

For the geometry shown in Fig. 4.2, there exists a single nonzero E-field component along the invariant (infinite) direction ($\hat{y}$), and two nonzero H-field components along the finite directions

($\hat{z}$, $\hat{x}$) which may be interpreted as either height or width [7]. Out of the three mathematically equivalent modes (TE^z, TM^y, TE^x), we choose the TE^z field configuration here, as it aligns best with the physical interpretation of the physical waveguide with propagation along $\hat{z}$ (length), a transverse E-field along $\hat{y}$ (width or height), and H-field components along $\hat{x}$ and $\hat{z}$. Our FDTD simulations are based on the traditional Yee algorithm in a 2D lattice, as formulated in ([20], ch. 3), where the formulation is derived with the assumption that $H_z = 0$ and $\partial_z = 0$, resulting in the TM^z mode with field components $\{E_z, H_x, H_y\}$. Note here that the E-field has a single nonzero component along the infinite (invariant) direction, and the H-field has two nonzero components. Since we can assign the FDTD geometry in an arbitrary manner, we choose to orient H_x along the length and H_y along the width (or height), resulting in a field configuration with the same orientation as the analytical formulation but with a rotated coordinate grid. We can rotate the coordinate grid of the analytical field configuration such that it results in a

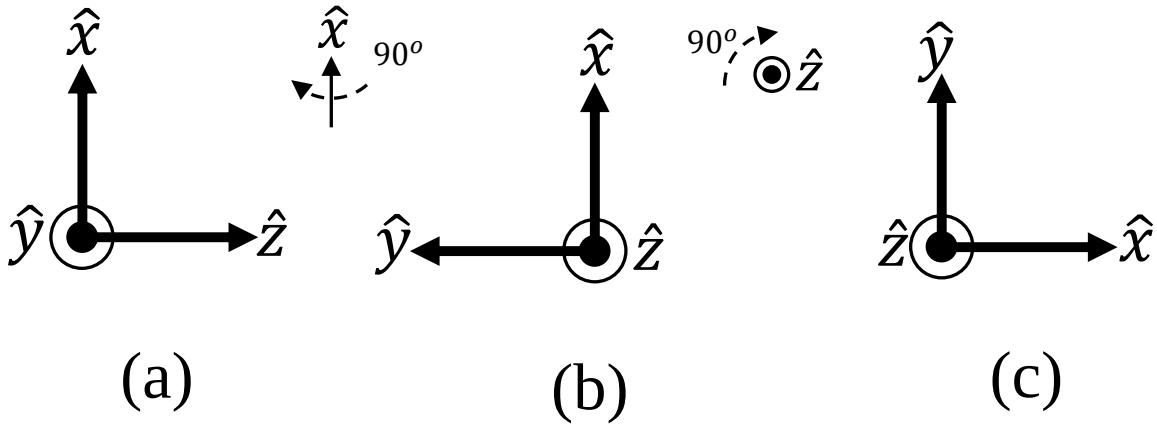

Figure 4.3: Coordinate grid rotation steps. (**a**) Initial orientation of analytical formulation for 2D TE^z. (**b**) Intermediary rotated mapping. (**c**) Final mapped orientation of analytical formulation is identical to the FDTD formulation for 2D TM^z. This figure was originally published in [5].

configuration *identical* to the FDTD fields by the steps shown in Fig. 4.3. In Fig. 4.3, starting with the analytical expression in (a), we rotate the coordinate grid twice. The first rotation is 90° around $\hat{x}$ from $\hat{z}$ toward $\hat{y}$; this produces the grid in (b). The second rotation is 90° around $\hat{z}$ from $\hat{y}$ to $\hat{x}$; this produces the grid in (c). The mapping is complete after these rotations, and we can then use the FDTD 2D TM^z field components $\{E_z, H_x, H_y\}$ to represent the analytical 2D TE^z field components $\{E_y, H_z, H_x\}$, respectively, with no modifications to the established FDTD formulation nor the analytical formulation.

4.1.4 Simulation Space Verification

We validate the FDTD model being used in these numerical experiments in three ways, described below. Unless stated otherwise, the data in this section is generated for a smooth

waveguide with $\delta = 300$ nm, $n_1 = 3.5$, $n_2 = 1.5$, and $f_0 = 194.8$ THz. Validation must be done prior to performing numerical experiments, so we utilize the smooth waveguide and the below methods for model validation. Using known and expected attributes of the smooth waveguide, we can compare the results obtained from numerical experiments to provide confidence in the validity of our model before performing numerical experiments with waveguides that exhibit surface roughness.

Wave Impedance One such method is through comparison with a known analytical solution to the smooth DSW. We use the wave impedance of an outward traveling wave. This solution is well established and has been derived in several places [7, 23]. We find the wave impedance by dividing TE^z mode E-field by the corresponding H-field component along the length of the DSW. Here, those fields are E_y and H_z, respectively. In the smooth DSW case, the real portion of the wave impedance should be very small. For the analytical solution, the division between the E-field and H-field gives

$$Z_w = \jmath \frac{x}{|x|} \frac{\omega\mu}{\gamma} \quad (\Omega), \tag{4.1}$$

where μ is the magnetic permeability. Division of x by its magnitude is used to set the appropriates sign for either above or below the DSW.

The FDTD portion of this comparison may be conducted through the second simulation from Chapter 3 with the surface roughness omitted. Since the wave impedance is calculated for an outward traveling wave, we use the E-field and H-field data in the cladding region. We take all the steps necessary to compare frequency-domain voltages as described in Section 4.1.2, but we exclude the final integration such that we are left with field data for every point along the line at ports 1 and 2. Using the port 2 data allows for the wave to propagate over a long enough distance to be well-set into the lowest order mode. We take the measurements from two cells below the lowest core cell which leaves a single cell buffer between the core region and the cell used for this calculation. Finally, the imaginary component is compared to the analytical solution.

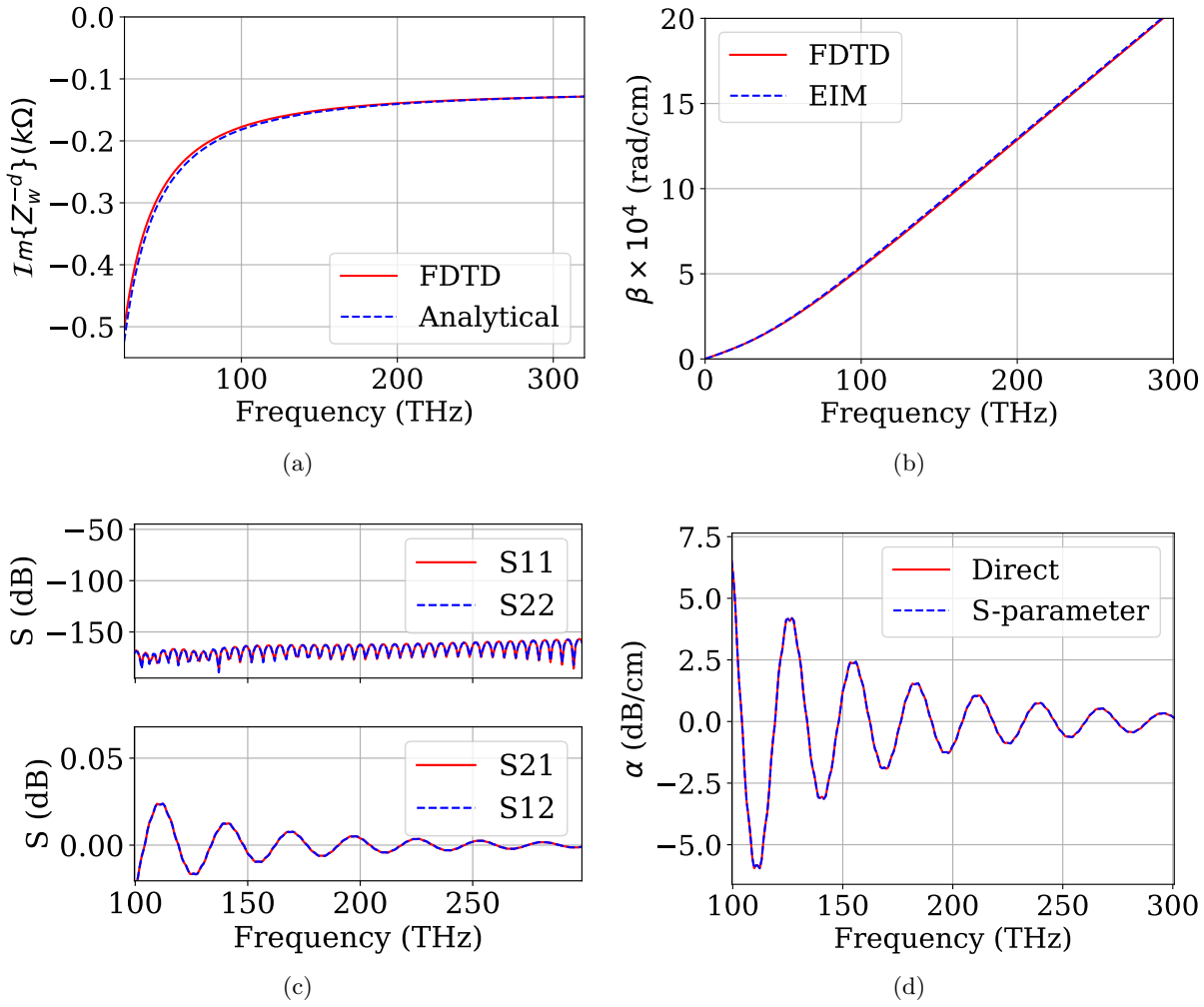

Figure 4.4: (**a**) Zeroth order TE^z mode wave impedance for the smooth DSW. (**b**) Propagation constant β vs. frequency. (**c**) S-parameters for the smooth waveguide. (**d**) Propagation loss α (dB/cm) vs. frequency, for a smooth waveguide with S-parameters method vs. direct method for calculating propagation loss. This figure was originally published in [5].

The wave impedance calculated from the FDTD model is shown in Fig. 4.4a. We can see that the impedance found from numerical experiment matches with the expected analytical value throughout this range of frequency samples. At f_0 the difference between the FDTD and analytical values is approximately 1.5 Ω, which translates to an error of less than 2% near the frequency of interest.

Propagation Constant In the next validation method, we compare the propagation constant β obtained from FDTD against that obtained from the EIM in the frequency range of interest, at the same samples as the FDTD model output. We find β from FDTD by evaluating the imaginary component of (3.4). Since we are examining the phase angle of the voltage measurements, the division of $\tilde{V}(\ell)$ by $\tilde{V}(0)$ may be converted to a subtraction, resulting in (4.2).

In FDTD, we compute the angle of the complex voltages over the entire frequency range on the smooth DSW and unwrap the final angle array into full angle form (rather than principal angle form). In Fig. 4.4b, the traces are nearly overlapped. The fundamental frequency is highlighted by the vertical dashed line, where the error between the EIM and the FDTD model is less than 1%. This data further validates the FDTD model, and confirms the formulation leading to (4.2).

$$\beta = -\frac{1}{\ell}\left(\arg\left(\tilde{V}(\ell)\right) - \arg\left(\tilde{V}(0)\right)\right) \tag{4.2}$$

Scattering Matrix In the last validation method, we utilize the properties of the S-parameters matrix described in Chapter 3. As stated, the matrix should be symmetric and unitary for the smooth waveguide. We extract the S-parameters from the FDTD model using the method presented in Chapter 3, and show these in Fig. 4.4c. Two observations are noteworthy in the frequency range of interest: (1) the cross-terms (S12, S21) have a magnitude of near 0 dB, indicating that there is almost complete transmission of power from one end of the waveguide to the other, and the self-terms (S11, S22) are correspondingly very small compared to the cross-terms, with a peak value of less than -150 dB; therefore, the matrix is nearly unitary as expected for a smooth lossless waveguide. (2) the S-parameter matrix is symmetrical, given the near perfect overlap of S11 with S22, and S12 with S21. These observations are the expected results for an ideal network, such as a smooth DSW. Since the FDTD results align well with the expected behavior of a 2-port network, these results further validate the FDTD model.

Scattering Loss Calibration We compare the *S-parameters method* and the *direct method* for calculating loss, as shown in Fig. 4.4d. Here, we observe an oscillatory behavior similar to that in the cross-terms of Fig. 4.4c. The oscillations hover around $\alpha = 0$ dB/cm and decay with increasing frequency, while the expected per-unit-length attenuation for an ideal smooth waveguide is $\alpha = 0$ dB/cm. Note that the loss from the S-parameters and from the direct method match very well, where the mean-squared error is on the order of 10^{-8}.

With an accurate model in hand, the field data are collected according to the methodology. In this manner, sample field data in the FDTD setup is shown in Fig. 4.5 and Fig. 4.6. The results shown in these figures are the electric and magnetic total field values evaluated at ports 1 and 2, according to simulation 2 of Fig. 3.2. Figure 4.7 shows the attenuation coefficient as a function of frequency using both the simple modal method as well as the S-parameter method. Note the error is negligible, as shown in Fig. 4.8. The overall S-parameters are shown in Fig. 4.9 and Fig. 4.10. As expected from a smooth dielectric waveguide structure in 2D FDTD, the attenuation is very small compared to the size of the simulation space, and power is almost fully transferred from port 1 to port 2. Additionally, S_{11} and S_{22} are negligibly small. Furthermore, the various methods for calculating the attenuation coefficient are nearly perfectly aligned.

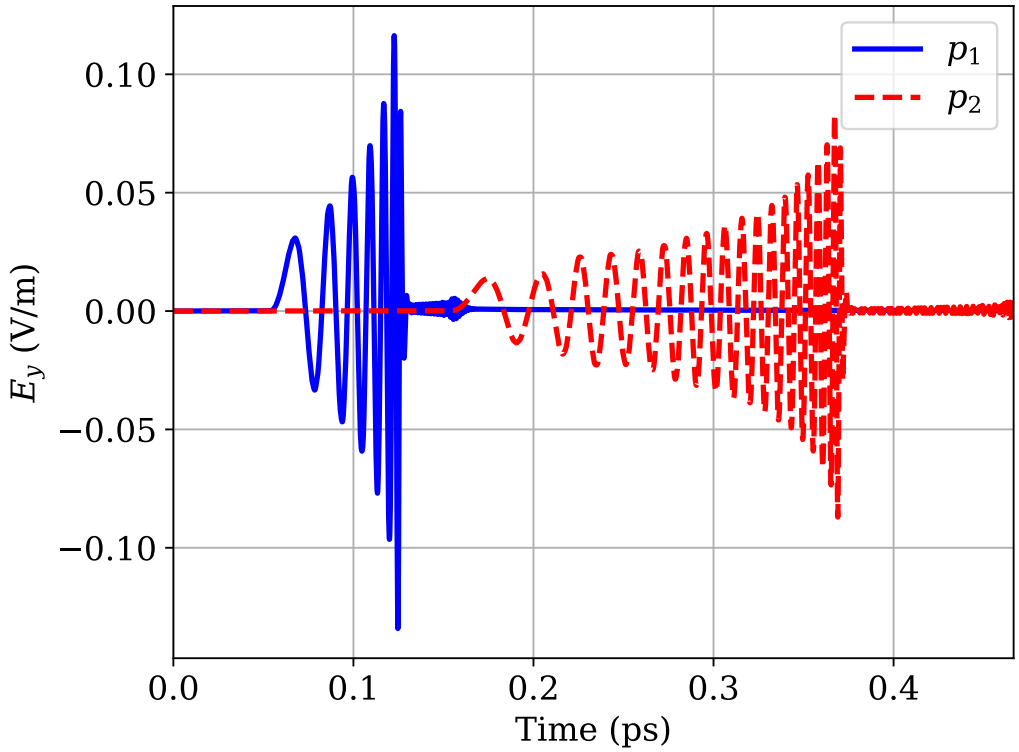

Figure 4.5: Electric field waveform samples at ports 1 and 2. This figure was originally published in [6]. ©2022 IEEE

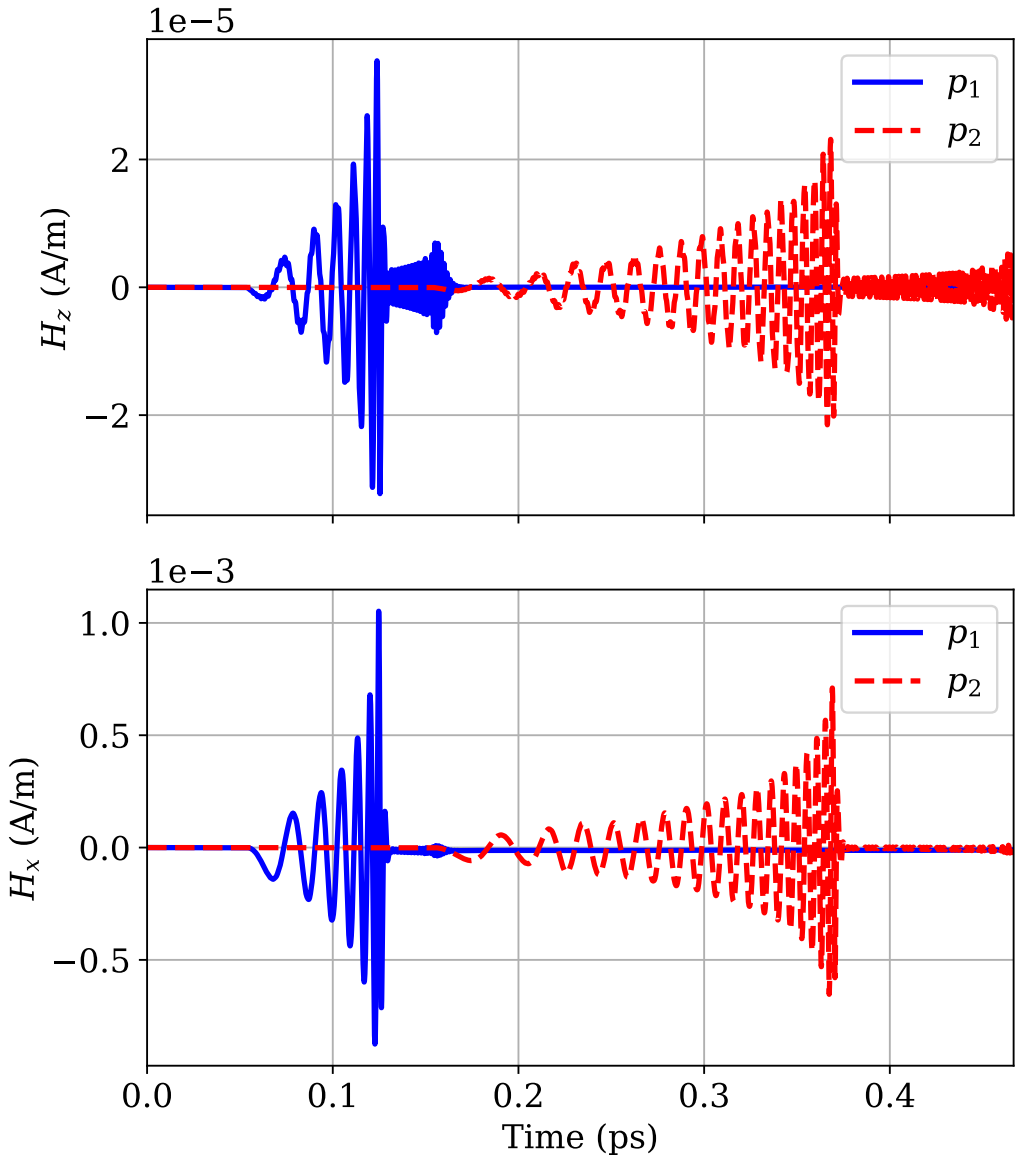

Figure 4.6: Magnetic field waveform samples at ports 1 and 2. This figure was originally published in [6]. ©2022 IEEE

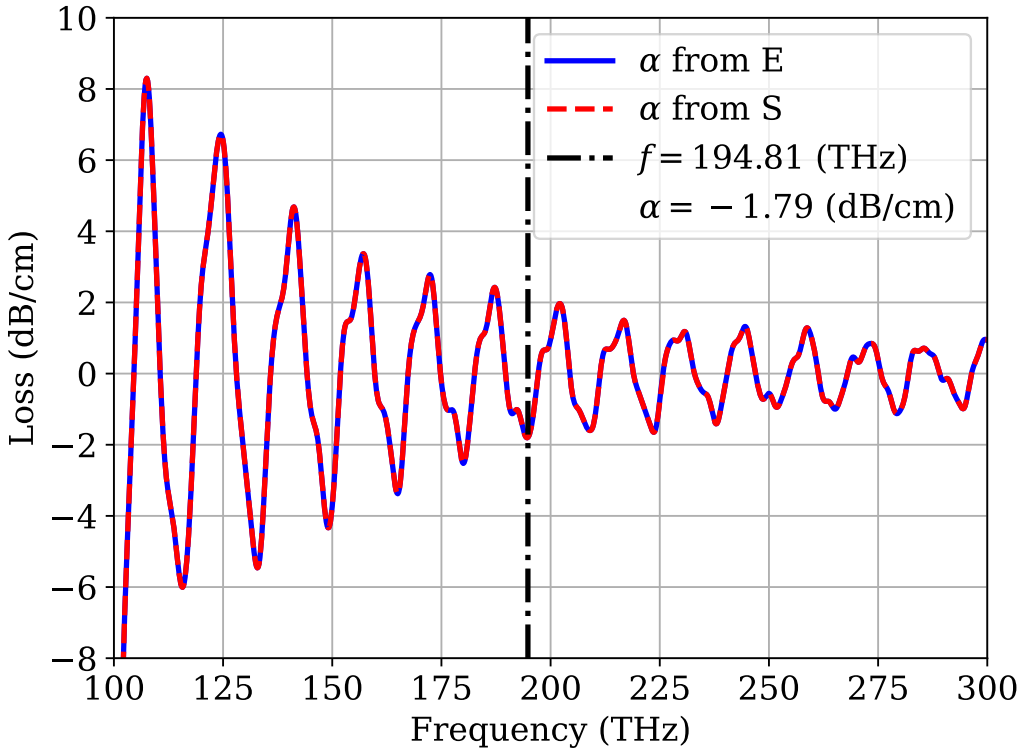

Figure 4.7: Comparison of α using (2.22a) vs. (3.7), including a numerical evaluation at $f = 194.81$ (THz). This figure was originally published in [6]. ©2022 IEEE

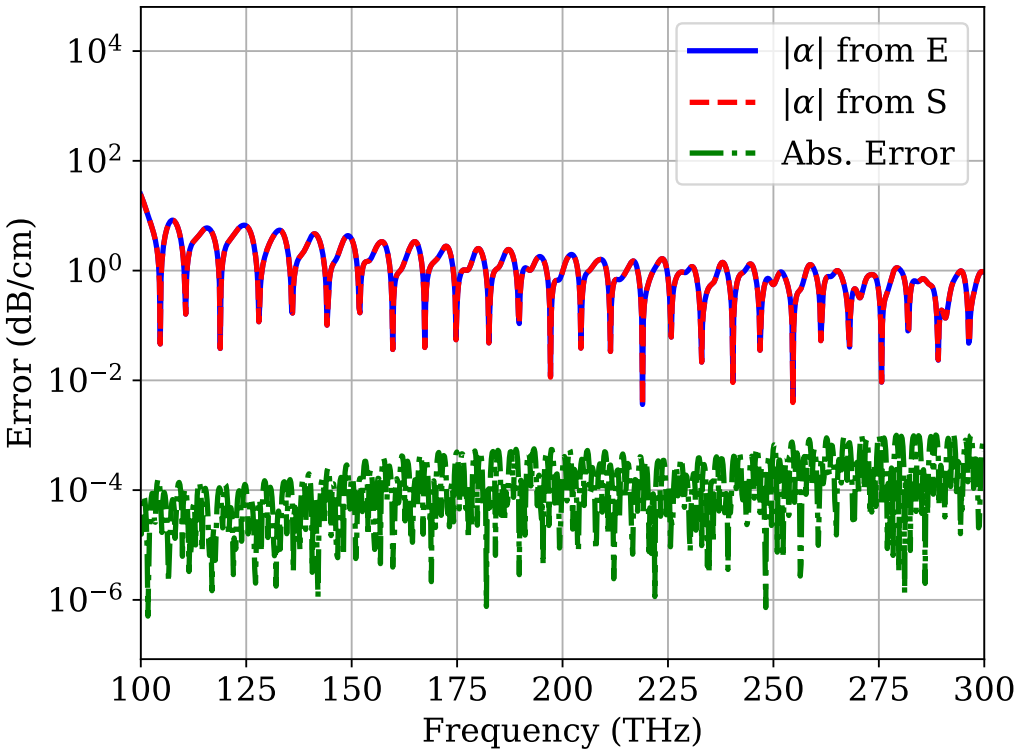

Figure 4.8: Magnitude of the absolute error (green) between the two methods presented here is compared with the magnitude of α using both methods. This figure was originally published in [6]. ©2022 IEEE

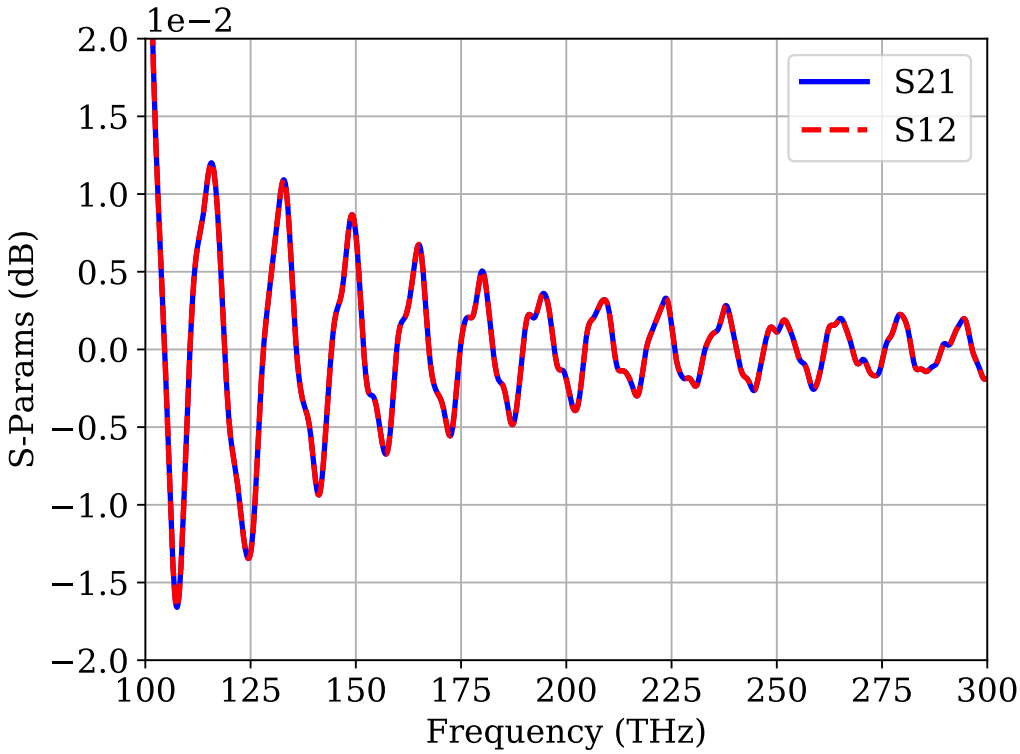

Figure 4.9: S-parameter cross-terms, showing the inherent symmetry of the structure. This figure was originally published in [6]. ©2022 IEEE

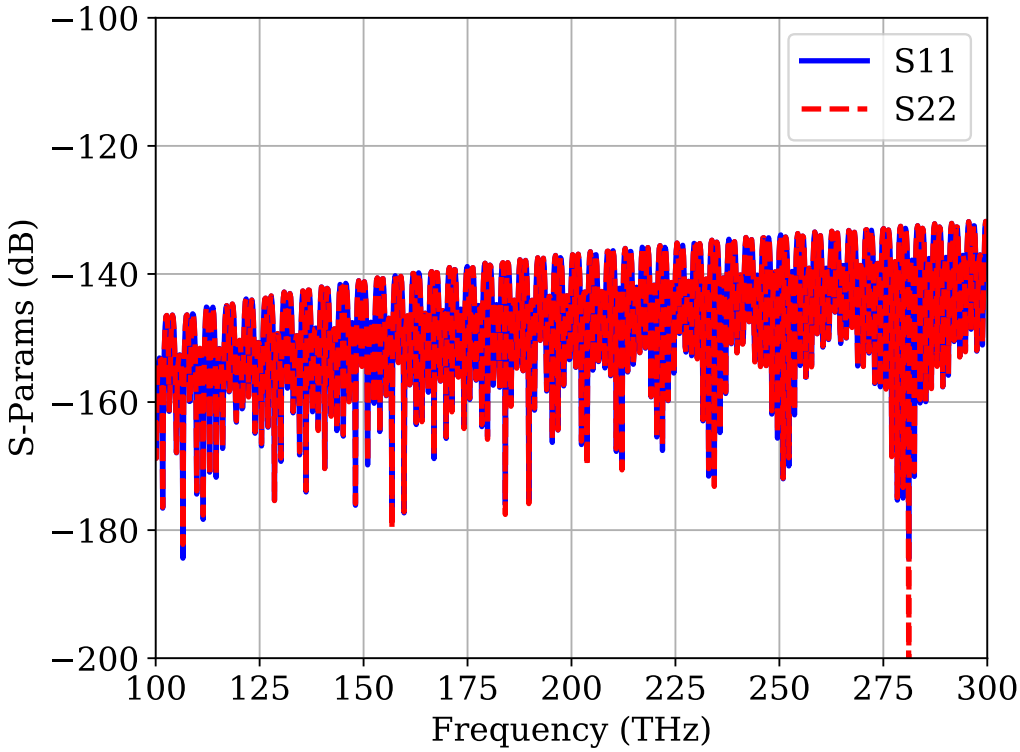

Figure 4.10: S-parameter self-terms, showing the low-loss nature of the structure. This figure was originally published in [6]. ©2022 IEEE

4.1.5 Correlated Profile Experiments

The FDTD method is used to solve a discretized DSW with stochastic sidewall roughness, where the upper and lower roughness profiles are identical (correlated). Correlated profiles are used to reduce numerical noise and show setup changes more distinctly. This setup is tested with $\sigma = 9$ nm and $\sigma = 15$ nm over a range of correlation lengths. The nominal loss value for each setup is calculated and converted to have units of dB/cm by multiplying loss in Np/m by 0.08686. This value is then compared against the computed loss value from FDTD. The minimum, mean, and maximum percentage difference from the expected loss value for each test-case is shown in Tables 1 and 2. In order to reduce some errors resulting from the stochastic nature of the problem, ten simulations are run for each setup. For each setup, a unique rough profile is generated, discretized, and evaluated for proximity to the setup conditions. Each profile is considered valid if the computed discrete parameters (σ, L_c) are within $\pm 10\%$ of the desired value. The evaluated discrete parameters are then used in the analytical calculation for each individual simulation, dependent on the true roughness profile experienced by the FDTD simulation.

$\sigma = 9$ (nm)

	Analytic	Error (%)		
Lc (nm)	α (dB/cm)	Min	Mean	Max
400	407.0	-11.19	11.60	23.51
500	339.2	-8.16	0.78	19.96
600	289.3	-21.82	-7.67	11.09
700	251.6	-29.20	-8.56	3.65
800	222.3	-15.19	0.99	12.06
900	198.9	-25.30	6.24	42.85
1000	179.9	-24.79	-1.91	22.53

Table 1: Results for $\sigma = 9$ (nm). α is the analytic value for the corresponding setup. Mean of mean errors is: 0.21%. Data within this table were originally published in [9]. ©2022 USNC-URSI

The average of the mean of the mean errors across L_c for both $\sigma = 9$ nm and $\sigma = 15$ nm is approximately -0.38%, showing a reasonable correlation between the numerical experiments in FDTD and the analytical solution. It may be noted that while ten simulations per setup can provide a rough trend, adding many more simulations for each test case would help increase statistical confidence in the correlation between analytical and FDTD results.

In Fig. 4.11, we show an example loss curve simulated in FDTD, to demonstrate the effectiveness of filtering the FDTD output. As we can be seen in the figure, there is a nontrivial level of noise on the full range of α. Applying a 10-point moving average filter results in the *Filtered* trace reduces the noise in the FDTD data. This is best exemplified by the α values for

$\sigma = 15$ (nm)				
	Analytic	Error (%)		
Lc (nm)	α (dB/cm)	Min	Mean	Max
200	1726.0	11.18	19.01	25.70
300	1390.2	2.30	12.61	25.70
400	1130.4	-11.28	6.78	20.83
500	942.2	-25.01	3.97	15.73
600	803.7	-23.74	-5.34	16.17
700	699.0	-27.69	-3.94	11.33
800	617.5	-45.18	-13.05	17.17
900	552.5	-40.71	-15.51	15.88
1000	499.7	-30.64	-13.18	12.02

Table 2: Results for $\sigma = 15$ (nm). α is the analytic value for the corresponding setup. Mean of mean errors is: -0.96%. Data within this table were originally published in [9]. ©2022 USNC-URSI

frequencies above 225 THz, where the noise is reduced by an order of magnitude. However, the noise reduction in the range around f_0 is more limited.

Figure 4.12 uses the data from tables 1 and 2, to illustrate the distribution of percent error between FDTD and analytical calculations with and without filtering. The values are grouped by corresponding σ values across varying correlation lengths. Figures 4.12a and 4.12b the same data at $\sigma = 9$ nm, where 4.12b has a 10-point moving average filter applied. Likewise, the same occurs for Figs. 4.12c and 4.12d but at $\sigma = 15$ nm instead. The figures show the distribution of percentage errors for all correlation lengths with the same standard deviation, where a total of 924 roughness profiles were simulated using the FDTD model. We use these data to illustrate the effect of filtering on simulation results. In Fig. 4.12a the mean error is -5.12%, whereas in Fig. 4.12b the error is reduced to -4.12%, and the standard deviation reduces from 21.96 to 19.87%.

In Fig. 4.12c the mean error is 1.89%, whereas in Fig. 4.12d the error is increased, to 2.24%. Like in the $\sigma = 9$ plots, the standard deviation reduces, this time from 19.76 to 18.56%. From the numerical experiments conducted in FDTD on the relatively short-length DSW, we have created the histogram of occurrences, which may be easily translated to a *probability mass distribution.*

Some potential sources of error in Fig. 4.12 are listed below. (1) The parameters $\{\sigma', L_c', \mu'\}$, rather than $\{\sigma, L_c, \mu\}$, are used in the analytical solution when calculating the percentage errors. (2) We use a relatively coarse spatial and temporal resolution in the FDTD model, while utilizing a finer resolution grid may decrease the percentage error range, it would increase computation time. (3) We use analytical model based on the formulation originally proposed in [14] that used various approximations and simplifications, such as a first-order Taylor series expansion to evaluate the E-field.

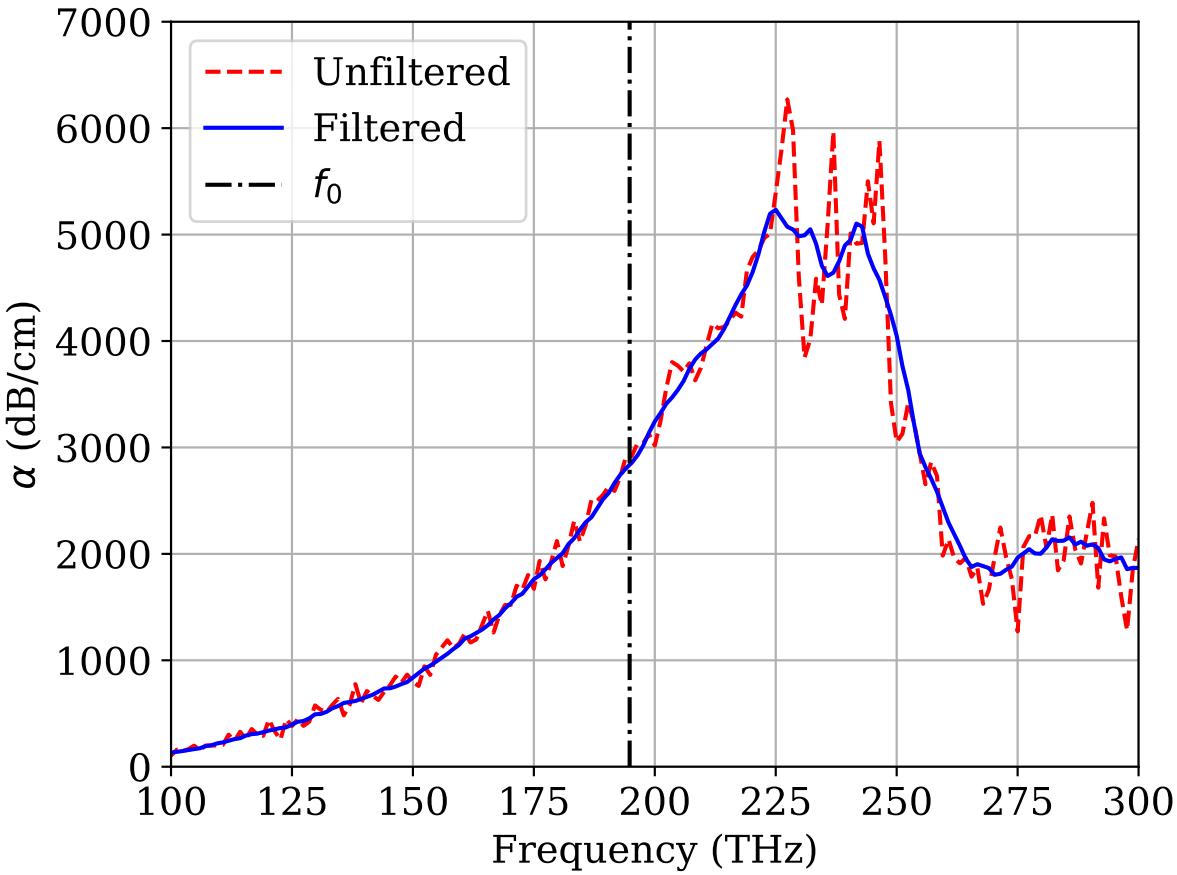

Figure 4.11: α vs. frequency, for a rough waveguide (σ = 15 nm, L_c = 200 nm) with noisy FDTD data (red dashed line) compared to filtered FDTD data (blue solid line), where f_0 is the excitation source frequency. This figure was originally published in [5].

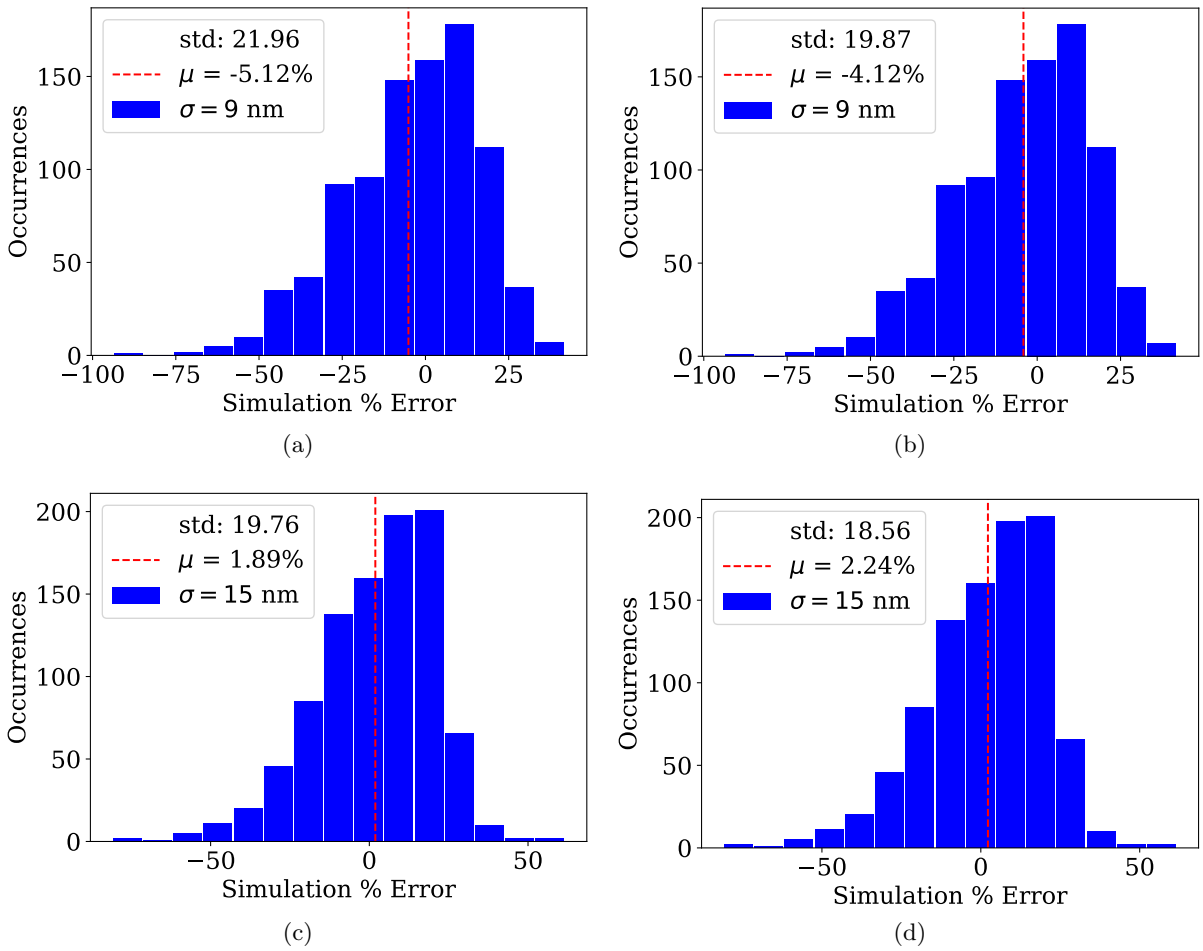

Figure 4.12: Percent error in propagation loss α (dB/cm) between analytical vs. FDTD solutions: (**a**) 924 roughness profiles at $\sigma = 9$ nm, (**b**) same as (**a**) with data filtering, (**c**) 947 roughness profiles at $\sigma = 15$ nm, and (**d**) same as (**c**) with data filtering. This figure was originally published in [5].

From each setup in Fig. 4.12 the maximum difference between filtered and unfiltered data is standard deviation from Fig. 4.12a,4.12b which reduces by 2.09%, and each other relevant value changes by around 1%, with the mean percentage error in the $\sigma = 15$ nm case actually increasing by 0.35%. This shows that the filtering step does not significantly impact the percentage error of the FDTD results from the analytical solution. Even in the best case, the differences between filtered and unfiltered data are minimal, and thus filtering is omitted from future experiments to improve the data integrity and increase the per-simulation computation rate.

4.1.6 Loss Value Comparisons

We compare this correlated profile experiment to previous theoretical and experimental works. In [7], the components for α are based on the more physically realistic form of E-field (2.1) where the peak amplitude A_e may be any real-valued scalar. The absence of any normalization factor (i.e., setting $N_F = 1$) leaves a dependency on input power; however, the input power may be modified to fit the expected scattering loss value for any point. In [14], the original formulation for finding scattering loss was proposed, where the mathematical normalization of (2.1) is used, effectively ignoring its contribution to the relationship.

The follow-up work of [16] proposed a formulation for scattering loss calculations by using normalized waveguide parameters, but as was noted in [15], there appears to be an extra factor of 2 in the formulation used therein. We can see this numerically by comparing [16] with this work, also in Table 3, where the loss value is double our calculations above. We further see that an input power of $P_{\text{TE}} = 4.3$ mW in the formulation found in [7] is most similar to the normalized values found here, but other choices of input power (e.g., $P_{\text{TE}} = 1$ mW or $P_{\text{TE}} = 1.45$ mW) could yield different values for loss as they may not eliminate dependence of α on input power. The VCM was used in [15] to verify the scattering loss calculations. Their work was done on several 3D waveguides, and these provide a similar analogue to the 2D structure simulated in this work.

Source (a: hardware experimental) (b: numerical/analytical)	$d = 210$ nm $L_c = 20$ nm $\sigma^2 = 1$ nm^2	$d = 250$ nm $L_c = 50$ nm $\sigma^2 = 81$ nm^2
a [13] Lee	N/A	≈34
a [10] Jaberansary	N/A	≈33
a [12] Horikawa	≈0.5	N/A
b [15] Barwicz	N/A	48.6
b [16] PL 94	1.87	193.7
b [7], $P_{\text{TE}} = 1$ mW	0.22	22.1
b [7], $P_{\text{TE}} = 1.45$ mW	0.32	32.1
b [7], $P_{\text{TE}} = 4.3$ mW	0.94	95.2
This work (2.8) (2.9b)	0.94	96.8

Table 3: α values in (dB/cm). Data in this table were originally published in [5].

Looking at the experimental side, in [12] a physical 3D dielectric optical interconnect was tested for scattering loss. Their results show that the 2D planar model [16] is generally an *overestimate* of what can be expected from physical hardware, and the 3D simulations in [15] are generally an *underestimate*. Furthermore, in [12], unit variance is used, making it unique compared to other experimental data and included in Table 3. Other experiments conducted on physical hardware include those of [10, 13], where a scattering loss magnitude of ≈35 dB/cm is reported. These experiments were conducted on 3D SOI optical interconnects consisting of Si core and SiO_2 cladding extending 1 μm in each direction around the core, making them amenable to comparison with the 2D planar approximation. The loss value in [10, 13] is approximately 36% of ours, and 72% of the loss value in [15].

4.1.7 Uncorrelated Profile Experiments

We simulated DSWs with rough surface profiles over a range of σ and L_c values. Each simulation generates unique roughness profiles for both the upper and the lower core/cladding boundaries. The simulation setups are each combination of $\sigma \in \{9, 15\}$ nm and $L_c \in \{200, 300, ..., 1000\}$ nm. 2168 waveguides were simulated (approx. 120 simulations per setup). We control for potential mismatch between simulation results and (2.8) by evaluating σ and L_c for each rough surface profile in that set, followed by taking the mean those σ and L_c values, and using those in (2.8). The error for each setup is calculated using (4.3).

$$\%E = 100 \times \frac{\alpha_{\text{analytical}} - \bar{\alpha}_{\text{simulation}}}{\alpha_{\text{analytical}}}, \tag{4.3}$$

where $\alpha_{\text{analytical}}$ is (2.8) and $\bar{\alpha}_{\text{simulation}}$ is the mean scattering loss calculated from FDTD results with the corresponding setup using the direct method.

We use the assumption core impedance normalization factor (2.9b) to calculate the error between (2.8) and simulation results, and we show those errors in Fig. 4.13. We observe that 10 of the 18 setups have errors with magnitudes larger than 30%. This results in the average error being between -30% and -40%, where (2.8) underestimates the FDTD scattering loss for each setup. Next, we use the effective impedance normalization factor (2.9a) to perform a similar error comparison between (2.8) and simulation results in Fig. 4.14. With this assumption the errors are reduced significantly. The latter normalization factor still underestimates the evaluated simulation scattering loss, but not to the same extent as with the former. Now, 10 of the 18 setups have errors with magnitudes smaller than 10%, and the average error is between -5% and -10%.

In Figs. 4.13 and 4.14, the errors from simulations with $\sigma = 9$ nm generally have a larger magnitude than those from $\sigma = 15$ nm, and as L_c increases the errors appear to approach a range of values. These observations are likely due to the particular grid discretization used in simulation. In the previous section it was shown that the core impedance normalization factor results in a very small error, but here we show that the same assumption and comparison

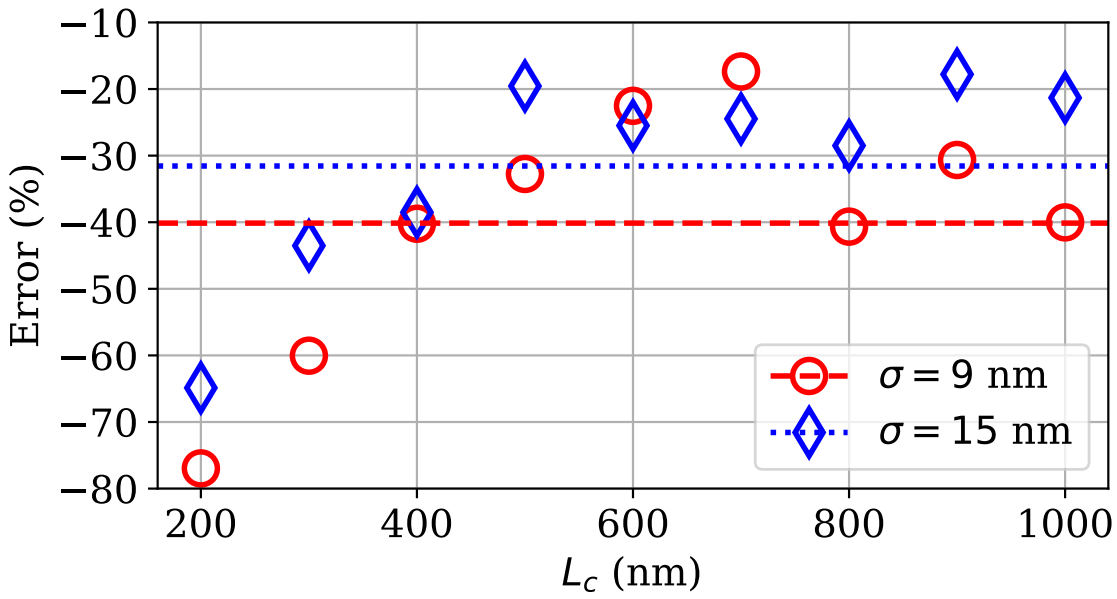

Figure 4.13: Percentage error for FDTD simulation results compared with (2.8), using normalization factor (2.9b). Markers show setup error. Lines show mean error for each σ. This figure was originally published in [1]. ©2022 USNC-URSI

results in a much larger error. This is because those simulations used *correlated* roughness profiles, i.e., the profile on the lower boundary is a direct copy of the profile generated for the upper boundary, whereas here the simulations use *uncorrelated* profiles, i.e., a unique profile is generated for both boundaries. In reality, correlated rough surface profiles are rare, so this experiment is much more realistic.

4.1.8 Setup Comparisons Data

Though the wave impedance shows good correlation with a relatively coarse discretization, rough waveguides may require finer detail to approach a similar closeness to analytical calculations. Through our numerical experiments, we found that primarily three variables affect stochastic simulations: (1) the resolution (number of divisions per defining wavelength), (2) rough waveguide length (ℓ), and (3) tolerance on discrete roughness parameters. Tests are performed in 2D FDTD, where

$$r \in \{20, 30, 40, 50, 60, 80, 100\},$$

$$\ell \in \{20\mu\text{m}, 30\mu\text{m}, 40\mu\text{m}\},$$

$$\mathcal{T}_p \in \{10\%, 15\%, 20\%\}$$

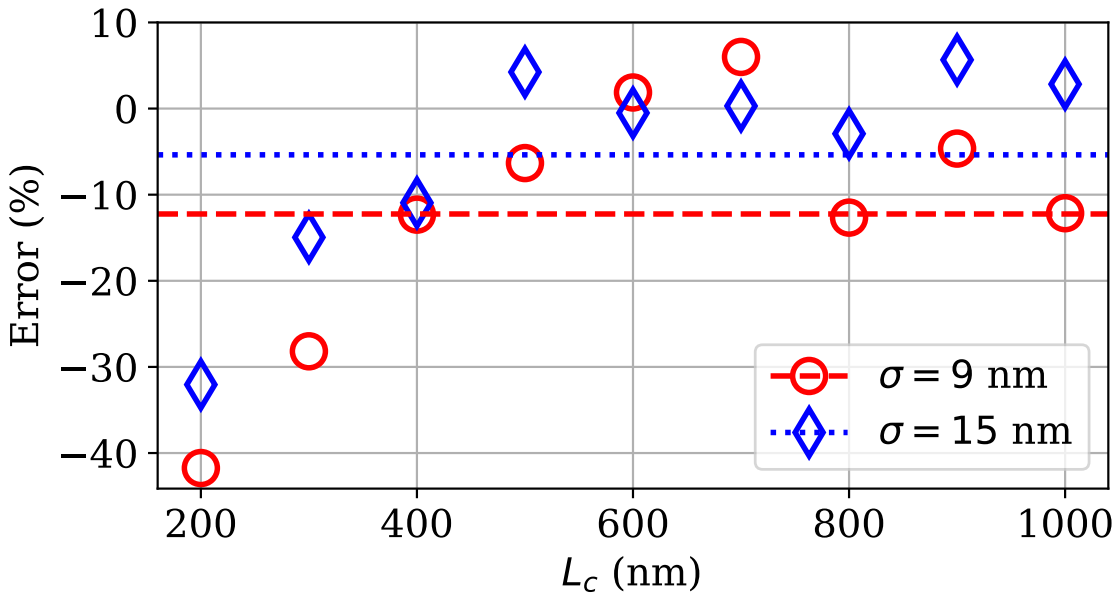

Figure 4.14: Percentage error for FDTD simulation results compared with (2.8), using normalization factor (2.9a) according to [7]. This figure was originally published in [1]. ©2022 USNC-URSI

are explored. Across all FDTD simulations for this experiment there were a total of 17,459 sample roughness profiles simulated (≈138 profiles per setup). The target roughness parameters are $\sigma_t = 15$ nm and $L_{c,t} = 500$ nm. This $L_{c,t}$ is near the center of the range of $L_{c,t}$ test setups in the subsequent experiments, but since the evaluation of (4.7) is not directly dependent on any particular $\sigma_t, L_{c,t}$, effectively any $\sigma_t, L_{c,t}$ could be used. Upon completion of all simulations for a particular setup, we take the mean and standard deviation of the resulting α values. These results are then processed further into percentage error and bandwidth defined in (4.4) and (4.5), respectively,

$$\%\text{error} = \frac{|\alpha_\text{A} - \bar{\alpha}_\text{F}|}{\alpha_\text{A}} \times 100\% \tag{4.4}$$

$$\%\text{BW} = \frac{\text{std}\,(\alpha_\text{F})}{\bar{\alpha}_\text{F}} \times 100\% \tag{4.5}$$

where $\bar{\alpha}_\text{F}$ is the mean of all FDTD α calculations for a particular setup, $\text{std}\,(\alpha_\text{F})$ is the standard deviation of those same calculated α values, and α_A is the analytical scattering loss evaluated at σ_t and $L_{c,t}$. We consider a setup to be *good* if the percentage error and bandwidth are both nearly 0%, where the ideal outcome implies high accuracy and high precision. We use (2.8) with normalization factor (2.9a) for α_A in Fig. 4.15, and we use (2.17) with normalization factor (2.18d) in Fig. 4.16. Results from TE^z mode simulations are shown in Fig. 4.15. Since profile generation is random and some test setups could result in an impossible combination, a cap

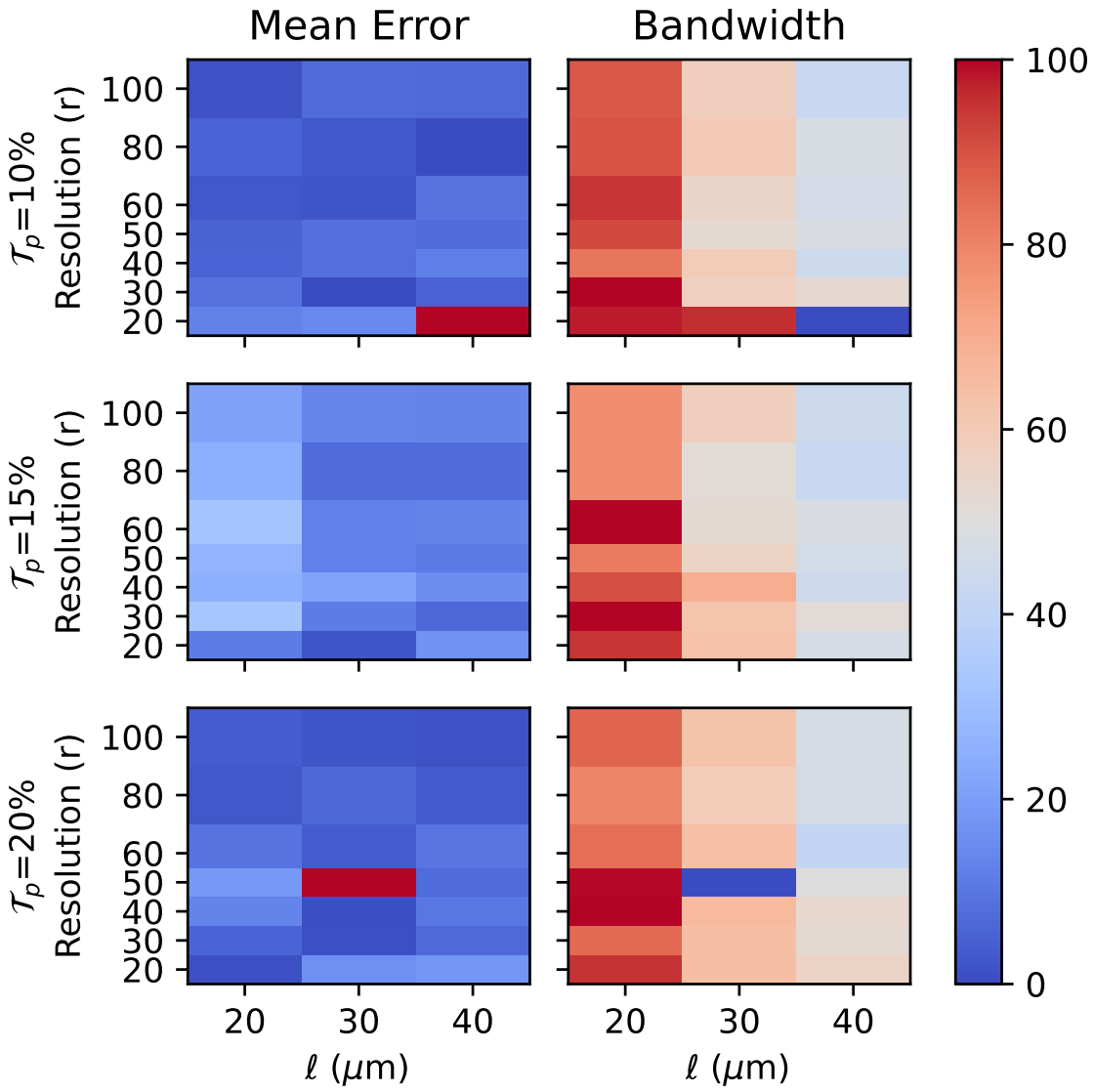

Figure 4.15: 2D TE^z mode results for r vs. ℓ vs. $\mathcal{T}_p$ at $\sigma_t = 15$ nm and $L_{c,t} = 500$ nm. This figure was originally published in [2].

for how many invalid roughness profiles may be discarded was set at 50,000. Should no valid profile be found over 50,000 iterations the setup is skipped and simulation of the next setup is started. The setups (ℓ, r, $\mathcal{T}_p$) = (40 μm, 20, 10%), (30 μm, 50, 20%) did not find any valid roughness profiles over 150 attempts (7.5×10^6 profiles were rejected for each). This may be seen in Fig. 4.15 as a mean percentage error of 100% and bandwidth of $\pm$0%. At least one valid roughness profile was found for all other setups in the TE^z mode.

The mean error decreases as ℓ and r both increase, so the best simulation results occur at (ℓ, r) = (40 μm, 100), however those results are only marginally better than at (ℓ, r) = (40 μm, 40) or (ℓ, r) = (30 μm, 50). In fact, any setup where the resolution and length are greater than at the aforementioned references seems to perform comparably well. Since the results only marginally improve for larger setups, we may assume that any setup with larger r or ℓ will primarily serve to increase the computation time rather than offer any improvement in comparison to analytical solutions. This serves to show that increasing the computational size is not necessarily beneficial to the accuracy of stochastic simulation.

The bandwidth for all TE^z mode sims appears to follow the same trend as the mean error, where some of the best results occur near (ℓ, r) = (40 μm, 100), but the benefit of increasing length is more distinct. We see a decrease in bandwidth of nearly $\pm$20% for each setup where ℓ is increased by 10 μm. However, this effect is not as readily seen with the increase in r. This implies that if r is large enough to adequately simulate the σ_t, there is little benefit to further increasing r. Conversely, even if ℓ is large enough to adequately simulate $L_{c,t}$, there is still visible and significant benefit to increasing ℓ.

Since the simulations are stochastic, no individual simulation should have exactly the same calculated α value as any other simulation, and while α may be similar between simulations, each roughness profile is unique. The range within which α may be expected to fall is dictated by the PDF that governs the roughness profile. The bandwidth decreasing from $\pm$60% to $\pm$40% by increasing ℓ from 30 μm to 40 μm has a benefit in that fewer simulations are required to reach a consistent mean value, i.e., a mean percentage error which changes minimally as more simulation results are added.

As $\mathcal{T}_p$ is increased we see a far subtler effect on α calculations, where the impact of $\mathcal{T}_p$ is most visible in the bandwidth. We see that a virtual *cutoff* point exists in the bandwidth plot for $\mathcal{T}_p = 20\%$ at $\ell = 30$ μm and $r = 50$. Below that point the bandwidth increases as r decreases, whereas the bandwidth is comparable to $\mathcal{T}_p = 10\%$ and $\mathcal{T}_p = 15\%$ as r increases. This implies that $\mathcal{T}_p$ has a similar but less significant effect to ℓ. This also shows that while $\mathcal{T}_p = 10\%$ will approach a marginally stable $\bar{\alpha}_\mathrm{F}$, $\mathcal{T}_p = 15\%$ does not necessarily require additional simulations to achieve a similar $\bar{\alpha}_\mathrm{F}$.

The results from TM^z mode FDTD simulation are shown in Fig. 4.16, where there are several differences between TE^z and TM^z mode FDTD simulation results. The setup at (ℓ, r, $\mathcal{T}_p$) = (40 μm, 20, 10%) again was unable to generate any valid profiles across the 150 search attempts, but (ℓ, r, $\mathcal{T}_p$) = (30 μm, 50, 20%) found at least one valid profile.

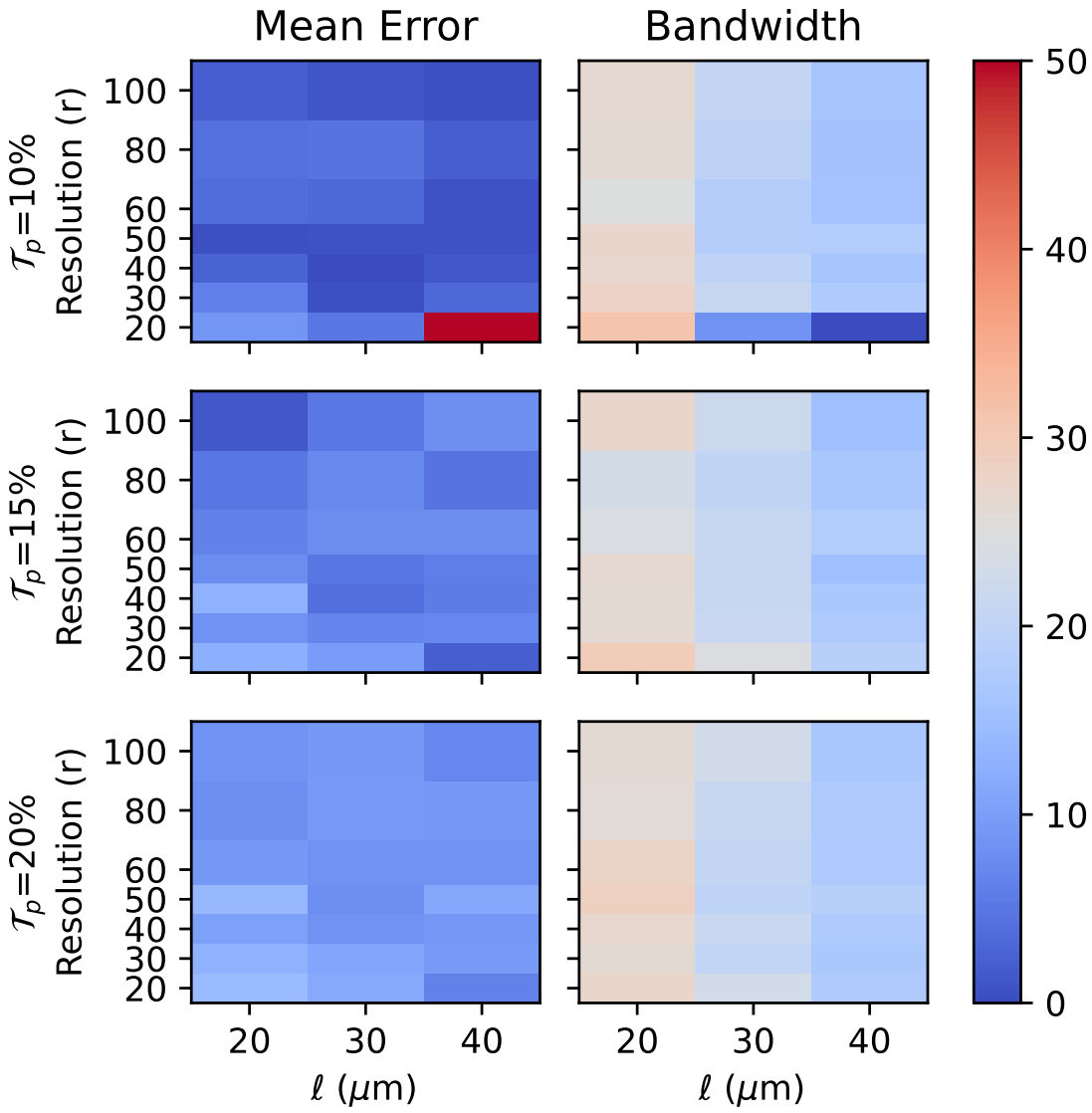

Figure 4.16: 2D TM^z mode results for r vs. ℓ vs. $\mathcal{T}_p$ at $\sigma_t = 15$ nm and $L_{c,t} = 500$ nm. This figure was originally published in [2].

Unlike the TE^z mode simulation results, the simulation results from TM^z mode simulations appear to be much less sensitive to the test parameters. However, the same trends are still present between the two modes. Once again, the best results are seemingly at the largest ℓ and r values and the smallest $\mathcal{T}_p$ values, but as ℓ increases we may see only a small decrease in mean error or in bandwidth for most results. Furthermore, there is an even smaller difference as r increases. The TM^z mode having a lower mean percentage error overall indicates that TM^z mode analytical model is less sensitive to changes in scattering due to surface roughness calculated during simulation. The lowered sensitivity is likely due to α_{TM} being larger than α_{TE}. This data contradicts the results found in [11], where the α_{TM} was approximately half α_{TE}, but here we see that $\alpha_{\mathrm{TE}} \approx 1170$ dB/cm and $\alpha_{\mathrm{TM}} \approx 3870$ dB/cm for this $\sigma_t, L_{c,t}$.

4.1.9 Statistical Analysis on 2D Stochastic Loss

We simulate stochastic roughness in the 2D TE^z and 2D TM^z modes. The data from those simulations are shown in Table 4, where all values for α_{F} are shown in dB/cm. The TE^z mode simulations were performed with $r = 60$ and $\ell = 80$ μm with $\mathcal{T}_p = 10\%$, and those in the TM^z mode were performed at $r = 60$, $\ell = 40$ μm, and $\mathcal{T}_p = 5\%$. These data are compared with

Mode	$L_{c,t}$	sims	$\bar{\alpha_{\mathrm{F}}}$	std(α_{F})	min(α_{F})	max(α_{F})
TE	300	143	1898.97	331.26	1080.32	2723.35
TE	400	143	1466.58	301.35	563.65	2136.93
TE	500	142	1154.80	291.53	581.83	2172.36
TE	600	142	986.20	300.26	342.73	2172.36
TE	700	142	862.45	250.73	309.56	1692.91
TE	800	142	742.81	254.23	5.62	1484.56
TM	300	147	5058.42	862.97	2833.08	7164.78
TM	400	146	4482.29	837.37	2058.77	6403.92
TM	500	146	3912.81	796.84	1886.13	6252.10
TM	600	145	3456.58	796.28	1903.49	5287.46
TM	700	146	3045.63	696.56	1405.46	4660.05
TM	800	145	2683.57	641.75	1184.69	4474.81

Table 4: 2D Simulation Data. Data in this table were originally published in [2].

analytical equations across each of the normalization factors, where the TE^z mode is compared with (2.8) in Fig. 4.17 and the TM^z mode is compared with (2.17) in Fig. 4.18. Both are shown in percentage error with each respective analytical function and normalization factor.

Errors for specific L_c are shown as markers, and the mean error across all setups for a particular normalization factor is shown as an associated horizontal line. In these comparative figures, positive and negative percentage errors indicate whether the analytical function *overestimates* or *underestimates* evaluated FDTD data, respectively. The TE^z mode analytical solution needs the (2.9a) normalization factor to match well with simulation results, while the

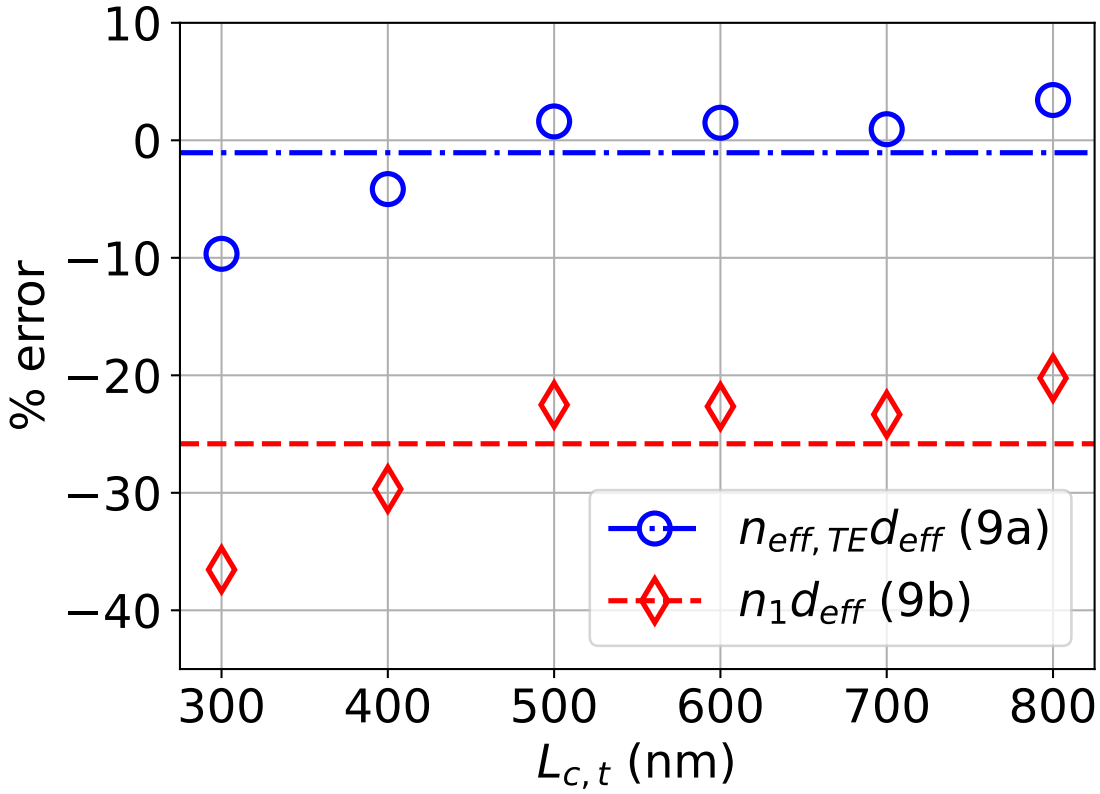

Figure 4.17: 2D TE^z percentage errors at (2.9a) and (2.9b). This figure was originally published in [2].

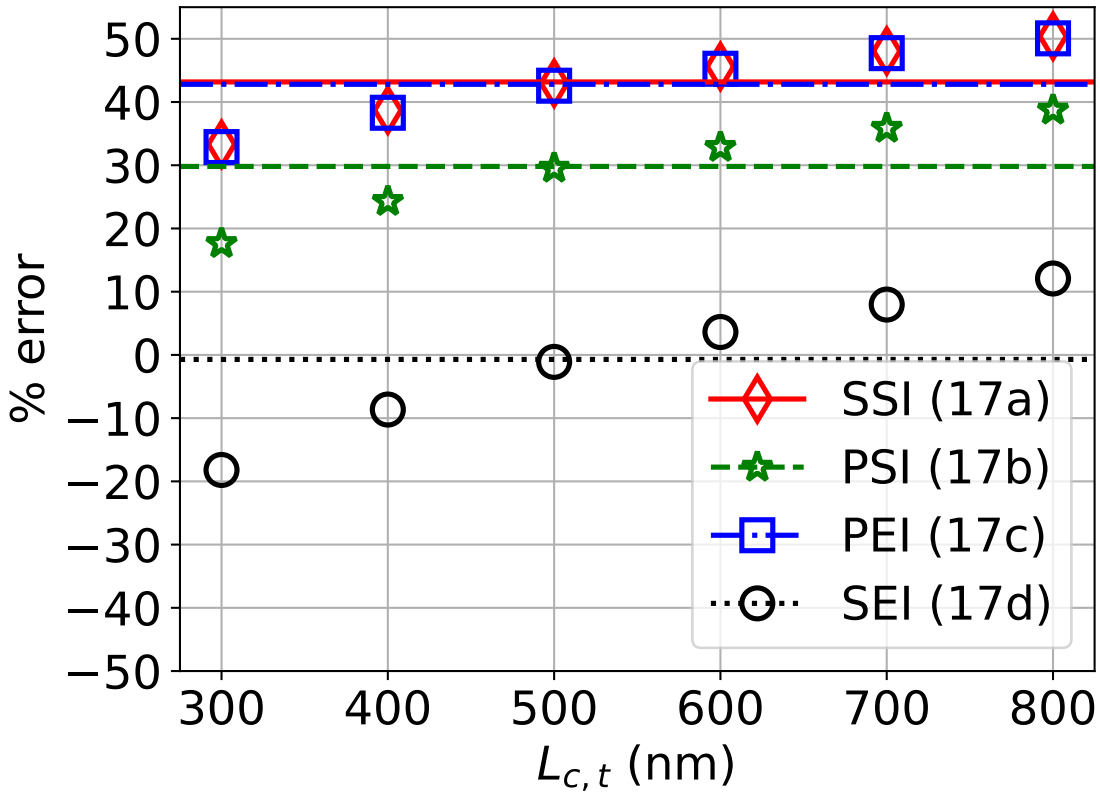

Figure 4.18: 2D TM^z percentage errors across all 4 options in (2.18). This figure was originally published in [2].

(2.9b) normalization factor greatly underestimates the evaluated loss figures as predicted in Fig. 2.1a. This further corroborates the results from [1, 5].

Fig. 4.18 shows some similarities to Fig. 4.17, but there are also some notable differences. While the analytical solution in the TE^z mode seems to tend toward underestimation with the (2.9b) normalization factor, the TM^z mode simulations show that the normalization factors other than the SEI option (2.18d) produce a large *overestimation* of simulation scattering loss values. *This is likely due to the inversion of η in the duality-based translation from TE^z to TM^z analytical functions.* In this comparison, the SEI option is clearly the best, with a mean error nearest to 0% and individual errors within ±20%. Despite the mean being close to zero in the SEI, there is a linear behavior in the point-to-point percentage errors not seen in the TE^z mode results, seemingly as a function of L_c. This linear behavior may be seen in each of the presented normalization factor options, where neither singular nor piecewise impedance corrects the offset.

It is possible to "correct" this offset for *any* of the four options by multiplying the analytical function by the correction factor (4.6)

$$C = 1 - \mathcal{M}L_c - b, \tag{4.6}$$

where $\mathcal{M} = \frac{\mathrm{error}_2 - \mathrm{error}_1}{L_{c,2} - L_{c,1}}$, and $b_i = (L_c - L_{c,i}) - \mathrm{error}_i$, and $i \in \{1, 2\}$, and points 1 and 2 designate a particular *relative* error (and not the percent-error) corner and L_c coordinate pair. This correction factor serves to highlight the absence of a higher-order L_c-dependence in the proposed analytical solution. This "correction factor" can only be used to highlight this point, and *cannot* correct actual data as that would nontrivially modify experiment results, thereby invalidating findings. Therefore, the correction factor is not applied in **any** other context.

4.2 3D FDTD Numerical Experiments: Results and Discussion

4.2.1 Simulation Setup

We test the analytical formulations using the FDTD method based on the traditional Yee algorithm [19,20,40] in 2D TE^z, 2D TM^z, and 3D. The coordinate transform outlined in section 4.1.3 may be used to translate the analytical notation to the 2D FDTD notation, but no such transform is required for 3D FDTD. The discretized geometry from Fig. 4.1 is shown in Fig. 4.19 and essentially adds the source and the boundary conditions; the three primary cross-sections (center-slices) for 3D FDTD are shown, where the 2D FDTD simulations use only Fig. 4.19a.

The spatial discretization (Δx) is uniform and proportional to the wavelength in the core region, where $\Delta x = \frac{\lambda_0}{r n_1}$, $r \in \mathbb{N}$ is the resolution, and λ_0 is the source wavelength in free-space, in both 2D and 3D simulation spaces. The temporal discretization is set at the Courant limit in the cladding region, i.e., $\Delta t = \frac{n_2 \Delta x}{c_0 \sqrt{D}}$, where $c_0 \approx 3 \times 10^8$ m/s and D is either 2 or 3 for the respective spatial dimension. The boundary conditions of all simulations are the *convolution perfectly matched layer* (CPML) [20, 21], where $N_{\mathrm{CPML}} = 20$.

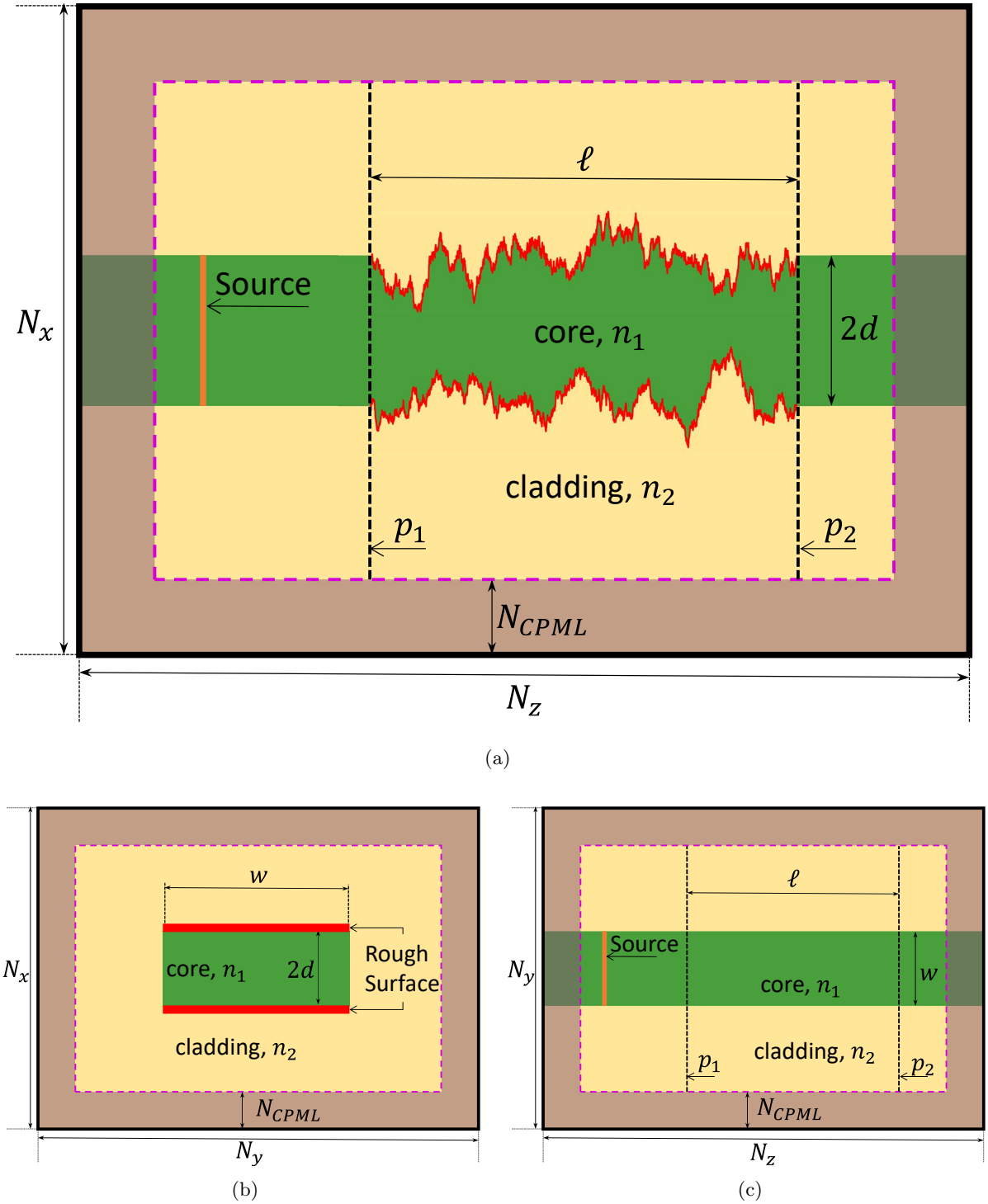

Figure 4.19: FDTD setup (a) $\hat{x} - \hat{z}$, (b) $\hat{x} - \hat{y}$, and (c) $\hat{y} - \hat{z}$ center-slice cross-sections. This figure was originally published in [2].

Figures 4.19a and 4.19c show both ends of the waveguide length are terminated fully into CPML. This ensures there is neither spurious resonance in the nominal geometry nor reflection from end-cap core/cladding boundaries. The fields outside the waveguide (along the transverse axes) decay exponentially, so the cladding region for those dimensions is sized such that the distance between the core and CPML regions is set to $2\lambda_0$ in 2D simulations and $0.55\lambda_0$ in 3D simulations. At these distances it is expected that little waveguide power reaches the CPML region in the absence of roughness.

The waveguide is excited for single mode operation. Both TE^z and TM^z modes are excited using the corresponding $\hat{y}$ source field-component uniformly over the entire mouth of the waveguide, as shown in Fig. 4.19a and 4.19c. The total simulated waveguide length is split into three regions; these are the (1) *settling*, (2) *rough*, and (3) *end* regions, where the settling and end ranges are smooth waveguide regions. The settling region is required for the excitation to enter into a *guided* mode. In 2D simulations this range was determined to be approximately $5\,\mu$m, and in 3D it was approximately $4\,\mu$m. The end range is needed to reduce noise for power calculations and is approximately 10 cells wide. The roughness is applied between the settling and end ranges, and power calculations are made at port locations p_1 and p_2, at one cell away on the exterior of the rough region along the waveguide length.

The analytical formulation is based on the assumption of *uncorrelated* upper and lower roughness profiles, so two rough profiles are generated randomly and discretized for each simulation involving roughness; in a process similar to that in described in [5]. We evaluate α in FDTD by calculating power at p_1 and p_2 according to (4.7)

$$\alpha = -\frac{1}{\ell} \ln \left| \frac{P(p_2)}{P(p_1)} \right|, \tag{4.7}$$

where power calculations are performed by numerically integrating along the waveguide cross-section between the lower and upper CPML boundaries. In 2D simulations we use the right-hand side of (2.7a) and (2.7b) for TE^z and TM^z modes (using only $|E_y|^2$ or $|H_y|^2$ and the corresponding η_g), respectively. We calculate power using (4.8) for 3D simulations

$$P_{g,3D} = \frac{1}{2} \int_{-\infty}^{+\infty} \int_{-\infty}^{+\infty} \Re \left\{ \left(\vec{E} \times \vec{H}^* \right) \cdot \hat{z} \right\} dxdy, \tag{4.8}$$

where $\pm\infty$ is approximated by numerically integrating between the CPML boundaries. All power calculations are evaluated at a single frequency, where the frequency-domain E-field and H-field are calculated using the *simultaneous fast Fourier transform* (SFFT) [40] at the source frequency (f_0) during FDTD simulation, where $f_0 = c_0/\lambda_0$ (Hz).

4.2.2 Computational Environment

The simulations performed for the subsequent experiments were computed with *graphical processing unit* (GPU) parallelization on NVIDIA RTX$^{\text{TM}}$ A6000 hardware. Computational speed for these simulations is evaluated with

$$\nu = \frac{N_x \times N_y \times N_z \times N_t}{t_s \times 10^6}, \qquad \text{(Mcells/s)}$$

where N_x, N_y, and N_z are the number of cells in the simulation space along the $\hat{x}$, $\hat{y}$ and $\hat{z}$ directions, respectively, N_t is the number of time steps, and t_s is the total simulation time for each sample waveguide. In 3D FDTD, $\nu \approx 4500$ Mcells/s.

4.2.3 3D FDTD Environment Validation

We validate the FDTD simulation environment by calculating the *surface wave impedance* of the waveguide in the cladding region. This calculation is performed on a smooth waveguide, where the TE$^{\text{z}}$ and TM$^{\text{z}}$ mode wave impedances have analytical solutions (4.9a) and (4.9b), respectively,

$$Z_{\text{w,TE}}^{-d} = \frac{E_y}{H_z} = -\jmath\frac{\omega\mu_0}{\gamma_{\text{TE}}} \qquad (\Omega) \tag{4.9a}$$

$$Z_{\text{w,TM}}^{-d} = -\frac{H_y}{E_z} = \jmath\frac{\gamma_{\text{TM}}}{\omega\epsilon_2} \qquad (\Omega), \tag{4.9b}$$

where both impedances are calculated on the lower surface of the waveguide at $x = -d$. The field components are evaluated three cells below the waveguide core region at midpoint of the simulation space along the waveguide length. The cell offset ensures there is no ambiguity in ϵ. Note that the wave impedance of the smooth waveguide is purely imaginary for propagating waves in both TE$^{\text{z}}$ and TM$^{\text{z}}$, showing that it is lossless. This implies that any loss calculated during rough simulations must be the result of scattering from stochastic roughness. Also note that $Z_{\text{w,TE}}^{-d}$ is negative (capacitive) near the source frequency whereas $Z_{\text{w,TM}}^{-d}$ is positive (inductive). In 3D FDTD we additionally evaluate at midpoint along width, noting that the 2D analytical surface wave impedance is a good approximation for $w \gg h$.

Wave impedance results are shown in Fig. 4.20. Those data were collected as time-domain field components which were then converted to frequency-domain by the fast Fourier transform (FFT) [39]. The frequency-domain field components were then used with (4.9a) and (4.9b) to calculate wave impedance, where those results are shown as squares for 2D FDTD and circles for 3D FDTD. The resolution for wave impedance simulations was $r = 40$, and the total length was the settling region plus 10 μm for both 2D and 3D simulations. Fig. 4.20 shows near-perfect overlap between FDTD and analytical results in the frequency band of 100 to 300 THz, where the maximum difference between FDTD results and analytical calculation is less than 2% at $f = f_0 \approx 194.8$ THz. These results provide high confidence about our FDTD simulation methodology.

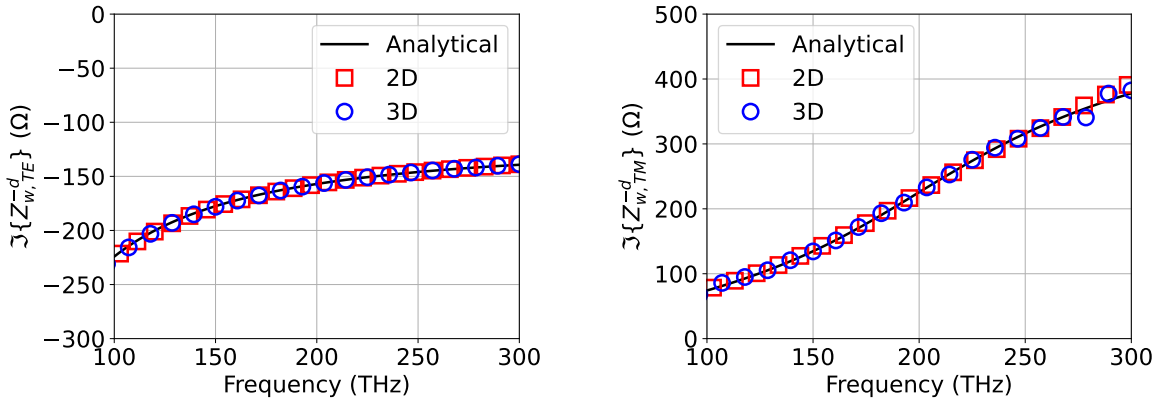

(a) (b)

Figure 4.20: Wave Impedance in the (a) TE^z mode and (b) TM^z mode. $\Im\{x\}$ is the imaginary part of x. This figure was originally published in [2].

4.2.4 3D Stochastic Roughness Analysis

The 3D simulation data are shown in Table 5, where all simulations were performed with $r = 40$, $\ell = 40$ μm, and $\mathcal{T}_p = 10\%$. The same comparisons performed for the 2D data are made again

Mode	$L_{c,t}$	sims	$\bar{\alpha_F}$	std(α_F)	min(α_F)	max(α_F)
TE	400	52	1487.96	152.71	1113.70	1820.25
TE	500	52	1209.86	176.19	825.71	1774.58
TE	600	52	970.59	132.59	640.02	1404.50
TE	700	59	878.72	111.44	603.86	1134.35
TM	400	100	4508.49	533.26	3377.23	6018.22
TM	500	100	3765.00	411.78	2916.86	4923.59
TM	600	100	3364.13	403.83	2363.11	4418.36
TM	700	100	2963.02	396.24	2219.94	4281.01

Table 5: 3D Simulation Data. Data within this table were originally published in [2].

in 3D with Fig. 4.21 for TE^z-like mode and Fig. 4.22 for TM^z-like mode simulations.

In both modes, α_A is based on the assumption of 2D geometry with no variation along width. We approximate this effect by making the width much larger than the height. The source in 3D approximates the 2D model with TE^z-like and TM^z-like modes using an excitation in the primary field component along the width, i.e., E_y in the TE^z-like and H_y in the TM^z-like modes, respectively. Simulations in 3D FDTD are far more computationally expensive, so a more limited range of 3D simulations were performed (compared to 2D FDTD) at $\sigma_t = 15$ nm and $L_{c,t} \in \{400, 500, 600, 700\}$ nm.

We see therein that, at these settings, the 3D FDTD simulation space produces results quite similar to the corresponding 2D FDTD models. A particular point of interest is the standard

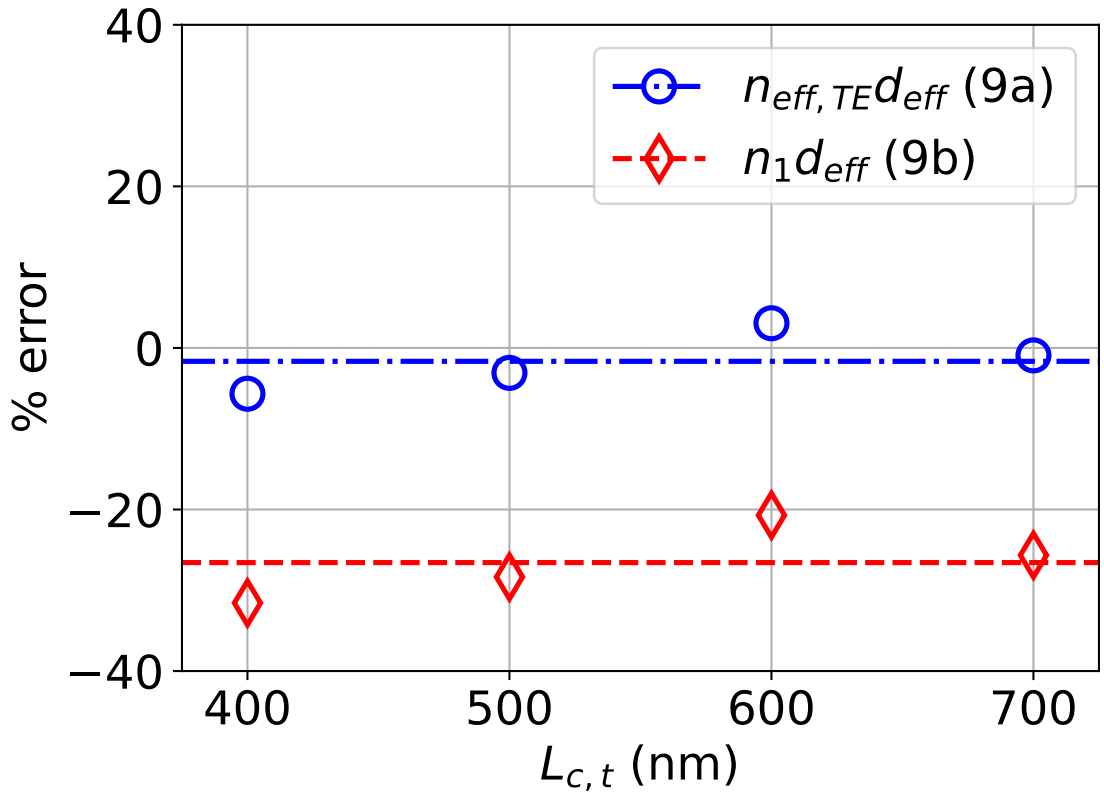

Figure 4.21: 3D TE^z percentage errors at (2.9a) and (2.9b). This figure was originally published in [2].

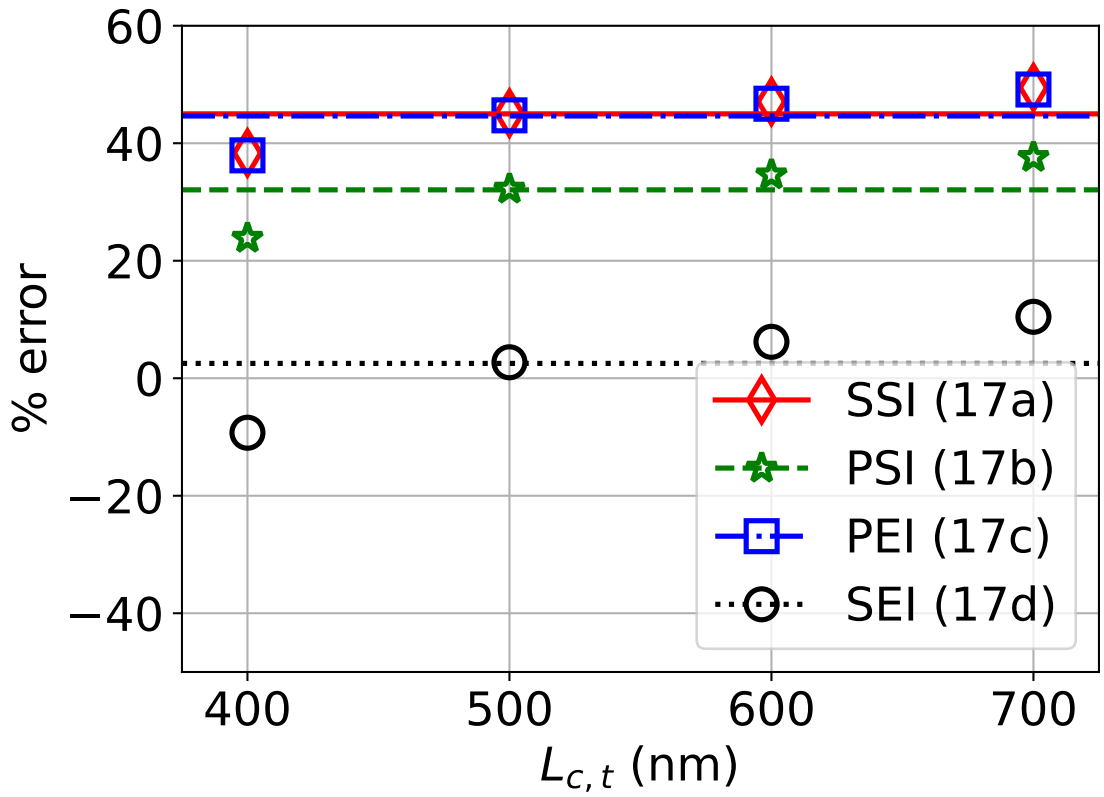

Figure 4.22: 3D TM^z percentage errors across all 4 options in (2.18). This figure was originally published in [2].

deviation of α_F, where the 3D FDTD simulations resulted in a smaller bandwidth compared to the 2D FDTD simulations by approximately a factor of two. This reduction appears to be the result of 3D versus 2D simulation spaces. There may be several possible explanations: (1) The rate and directions in which energy may spread in 3D simulation, i.e. spherical decaying (at $1/\rho^2$) as opposed to cylindrical decaying (at $1/\rho$). (2) The width confinement has some effect on more fundamental waveguide parameters, e.g., propagating mode cutoff frequencies, which affects the ability for certain wave patterns to propagate along the length. (3) 3D simulations provide a more robust environment for EM fields to exist and propagate, where energy exits the transverse plane, resulting in the dot product along $\hat{z}$ (used to calculate power flow along length) to capture only part of the guided power. (4) There could be more EM resonance which is not captured by the time-average power calculation, where energy exists but is not realized. While it is somewhat less noticeable than in the 2D case, the same linear behavior in the percentage error versus L_c shown in Fig. 4.22 may be seen. This may again be corrected using (4.6), but this has the additional computational burden of simulating a dimensionally larger space to obtain the data necessary for the computation of that correction factor.

4.2.5 3D FDTD Specific Considerations

The waveguides of interest are fully 3D and have step index contrast between core and cladding regions with refractive indices $n_1 = 3.5$ and $n_2 = 1.5$ (corresponding to Si/SiO_2), respectively, where the core is surrounded uniformly on all sides by a cladding which is assumed to be infinite in extent. The core region geometry is shown in Fig. 4.23, where we note the top and bottom walls of the waveguide are separated by the height (δ), the left and right walls are separated by the width (w), and all walls are smooth.

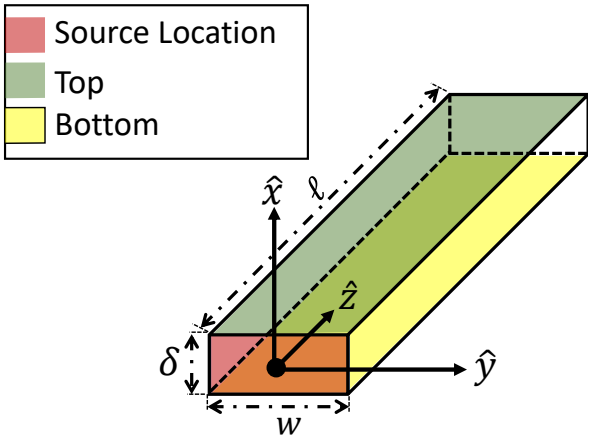

Figure 4.23: 3D waveguide geometry. This figure was originally published in [8]. ©2023 USNC-URSI

The 2D analytical Z_w model is defined in (4.10) [23] may be used as an approximation for comparison with 3D simulations data.

$$Z_w^{\mathrm{TE}} = \frac{E_y}{H_z} = -\jmath\frac{\omega\mu_0}{\gamma}, \qquad (\Omega) \tag{4.10}$$

The propagation constant can be evaluated from the relation of E-field components using the imaginary component of the complex logarithm in (4.11) [6]

$$\beta = \frac{1}{\ell}\left(\arg(E_1) - \arg(E_2)\right) = n_{\mathrm{eff}}k_0, \qquad (\mathrm{rad/m}). \tag{4.11}$$

For computing Z_w using (4.10), each numerical experiment uses $\lambda_0 = 1.54$ μm and $\delta = 200$ nm, and reported values are evaluated at $f = 194.8$ THz. FDTD field data are collected at the midpoints along ℓ and w, with a three-cell offset from the bottom of the waveguide core region.

These data are collected over widths varying from 200 nm to 5 μm. Those results are shown in Fig. 4.24. We see therein that Z_w calculated with FDTD approaches the 2D analytical model and saturates at $w \approx 800$ nm. There is a noticeable offset between the 3D FDTD data and the 2D analytical approximation below that point but little variation between FDTD and analytical

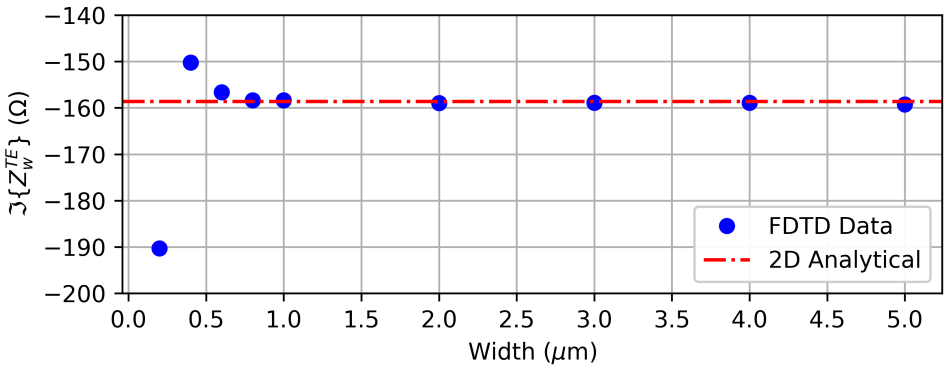

Figure 4.24: Z_w across widths. This figure was originally published in [8]. ©2023 USNC-URSI

calculations above that point. In this case, the 2D analytical model is a good approximation for $w \geq 4\delta$.

Sample FDTD Z_w data are shown with all discrete cells in the $w \times \ell$ cross-section in Fig. 4.25. The boundary of the region directly below the waveguide core is shown as dotted lines. Within the *below core* region there is minimal variation along length. Z_w settles to a stable value within 2 μm from the source location at $z = 0$, and the variations along w appear only near the region boundary. Outside the boundary there are several null points appearing periodically along length. The length interval between nulls seems to be inversely proportional to waveguide width. The null points are likely the result of 3D multi-modal behavior as more propagating modes exist in the waveguide with increasing w.

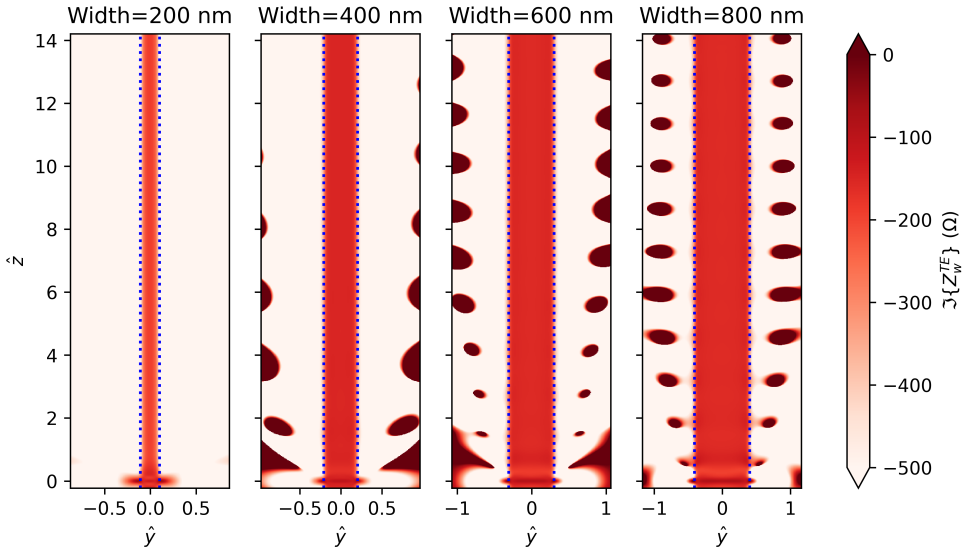

Figure 4.25: Z_w vs. w and length. This figure was originally published in [8]. ©2023 USNC-URSI

FDTD fields data are also collected at two $w \times \delta$ planes along length. The average of all E_y values in those planes is then related to β using (4.11), where $\ell = 5$ μm. We see saturation-like

behavior in Fig. 4.26 similar to Fig. 4.24. However, the saturation point for β appears to be at $w \approx 2$ μm. This implies that the 2D analytical model is a good approximation for the 3D

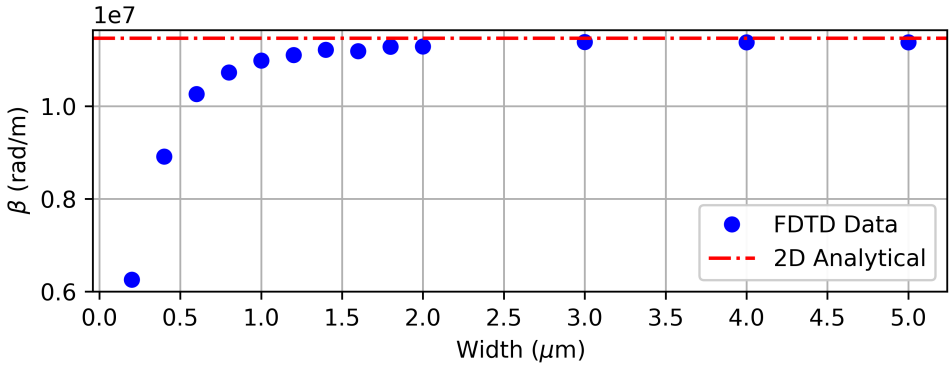

Figure 4.26: β across widths. This figure was originally published in [8]. ©2023 USNC-URSI

dielectric waveguide where $w \geq 10\delta$. Since Z_w is an implicit function of β through γ, this w limit should be used when utilizing the 2D analytical approximations. Fig. 4.27 shows the point-to-point β calculations (without field-averaging), where the boundary between core and cladding is shown as a red dotted line. The mode configuration changes as w increases, hence the use of field-averaging in Fig. 4.26.

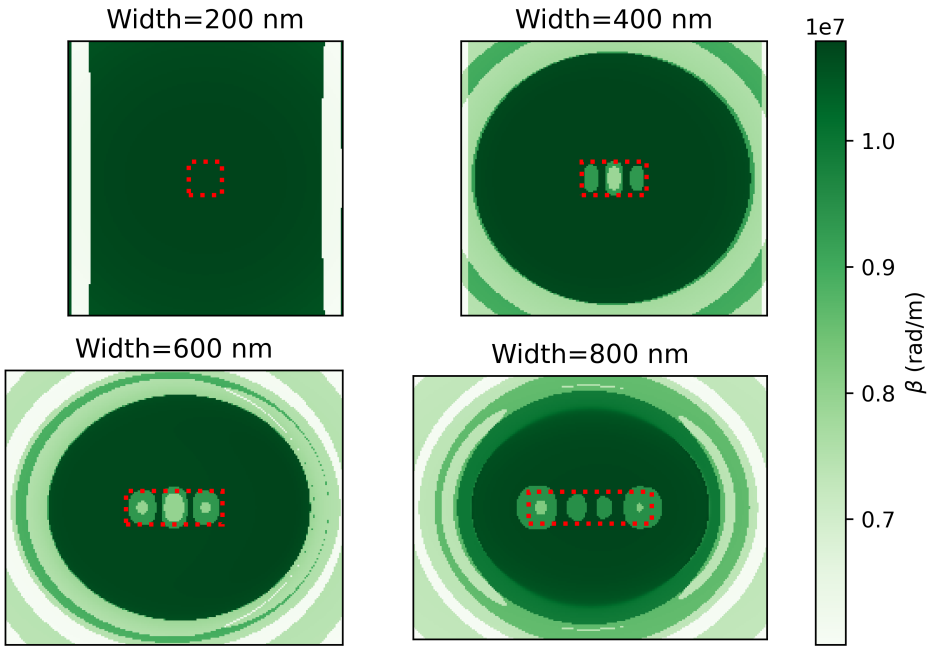

Figure 4.27: Point-to-point β across w and δ. This figure was originally published in [8]. ©2023 USNC-URSI

5 Conclusion

Text in this chapter originated from: [1–6, 8, 9].

While TE mode analysis of the stochastic propagation loss α in the DSW exhibiting random surface roughness on its sidewalls is prevalent [7, 14, 16], there has been little work done for the TM mode analysis of the same structure. Furthermore, comparison between 2D analytical model and both 2D and 3D computational models has been limited.

In this work, we **(1)** proposed a novel and simple analytical model for TM mode α of DSW, **(2)** provided several formulation options for guided-power normalization, and **(3)** compared those formulations against 2D and 3D FDTD simulations that revealed the proposed single effective impedance (SEI) as the optimal formulation. **(4)** A novel FDTD-based methodology for extraction of S-parameters for optical interconnects was proposed. Using the proposed methodology, the attenuation and the phase delay were calculated for a DSW operating in the mid-infrared regime. The results of the FDTD simulations were then shown to correlate well with known analytic solutions. **(5)**Additionally, we examined ways in which various normalization factors affect the guided power distribution across the height of the DSW, and highlighted the importance of normalization in both the TM and TE modes through stochastic numerical experiments in FDTD. **(6)** We swept several key FDTD parameters and monitored 2D FDTD performance to report the optimal settings required to achieve accurate stochastic results. We then used those settings to simulate hundreds of 2D and 3D rough waveguides at various target values for standard deviation σ and correlation length L_c. In that comparison we showed that the 3D FDTD simulation results match well with the 2D analytical model for this particular application of surface roughness. The proposed normalization factor in the TM mode is the dual to the best normalization factor in the TE mode. However, the TM mode exhibits a linear deviation in the α's percentage error between the analytical model and the 2D/3D FDTD models.

We note that while the 2D analytical models appear to be effective in predicting general trends in α of 2D and 3D FDTD, the 2D analytical models may need further refinement and increased complexity to provide higher accuracy, based on our data showing L_c-dependence of α in 2D and 3D FDTD. Additional numerical experiments are underway for analysis of α vs. 3D-specific parameters, such as finite width and an-isotropic surface roughness patterns, that affect comparison against the 2D analytical models.

The additional experiments conducted showed that fundamental parameters Z_w and β have a strong dependence on the w/δ ratio, where in this case, good correlation to 2D analytical model is achieved for $w \geq 10\delta$; the data suggests an order-of-magnitude difference would be sufficient.

The proposed analytical formulation of scattering loss was verified, using an expedient FDTD scheme which included extraction of the attenuation coefficient and S-parameters. We validated the FDTD scheme by comparing numerical results against previously published ana-

lytical functions for the DSW. With the FDTD model verified, we demonstrated S-parameters extraction and attenuation coefficient calculation by applying the proposed methodology to a smooth DSW. We then applied the methodology to compute the attenuation coefficient for a DSW exhibiting random sidewall perturbations according to the exponential autocorrelation function.

Along the way, we demonstrated the ability of the FDTD scheme to produce reasonably accurate results through tens of simulations for sidewall roughness profiles of varying correlation length at standard deviations of $\sigma = 9$ nm and $\sigma = 15$ nm. The FDTD results showed that the mean error for simulation is quite small, with an overall average error of only -4.12% and 2.24% for the attempted standard deviations, respectively.

The simulation models used in this work were released as an open-source software in the Optical Interconnect Designer Tool (OIDT) [18,36] under the GNU General Public License v3.0 [41]. This tool is both CPU and GPU parallelized, where GPU parallelization has computational speeds at $\nu \approx 4500$ Mcells/s.

Some future topics of research may include investigation of the following items **(1)** causes behind the FDTD-observed linear offset in the TM-mode percent error (4.6), **(2)** effects of finite-width confinement on α in 3D, **(3)** effects of an-isotropic surface roughness on α in 3D, **(4)** implementation of the discretized and truncated surface roughness profiles that better model the specified continuous roughness profile, **(5)** modeling of surface roughness using an unstructured FDTD grid, and **(6)** cross-coupling effects due to roughness in tightly-coupled 3D waveguides.

Bibliography

[1] Brian Guiana and Ata Zadehgol. Stochastic Loss in Dielectric Slab Waveguides Due to Exponential and Uncorrelated Surface Roughness. In *IEEE International Symposium on Antennas & Propagation & USNC-URSI NRSM Radio Science Meeting*, pages 1–2, Jul 2022.

[2] Brian Guiana and Ata Zadehgol. Analytical Models of Stochastic Scattering Loss for TM and TE Modes in Dielectric Waveguides Exhibiting Exponential Surface Roughness, and a Validation Methodology in 3D FDTD, techrxiv, doi: 10.36227/techrxiv.19799737.v1, May 2022.

[3] Brian Guiana and Ata Zadehgol. Stochastic FDTD Modeling of Propagation Loss due to Random Surface Roughness in Sidewalls of Optical Interconnects. In *United States Nat. Committee URSI Nat. Radio Sci.Meeting (USNC-URSI NRSM)*, pages 266–267, January 2021.

[4] Brian Guiana and Ata Zadehgol. Machine Learning for Rectangular Waveguide Mode-Identification, Using 2D Modal Field Patterns. In *2023 United States National Committee of URSI National Radio Science Meeting (USNC-URSI NRSM)*, pages 311–312, 2023.

[5] Brian Guiana and Ata Zadehgol. Characterizing THz Scattering Loss in Nano-Scale SOI Waveguides Exhibiting Stochastic Surface Roughness with Exponential Autocorrelation. *Electronics*, 11(3), 2022.

[6] Brian Guiana and Ata Zadehgol. S-Parameter Extraction Methodology in FDTD for Nano-Scale Optical Interconnects. In *15th International Conference on Advanced Technologies, Systems and Services in Telecommunications*, pages 1–4, October 20-22 2021.

[7] Ata Zadehgol. Complex s-Plane Modeling and 2D Characterization of the Stochastic Scattering Loss in Symmetric Dielectric Slab Waveguides Exhibiting Ergodic Surface-Roughness with an Exponential Autocorrelation Function. *IEEE Access*, 9:92326–92344, 2021.

[8] Brian Guiana and Ata Zadehgol. Width Confinement in 3D Dielectric Waveguides and Comparison to 2D Analytical Models. In *2023 United States National Committee of URSI National Radio Science Meeting (USNC-URSI NRSM)*, pages 313–314, 2023.

[9] Brian Guiana and Ata Zadehgol. FDTD Simulation of Stochastic Scattering Loss Due to Surface Roughness in Optical Interconnects. In *2022 United States National Committee of URSI National Radio Science Meeting (USNC-URSI NRSM)*, pages 1–2, Jan 2022.

[10] E. Jaberansary, T. M. B. Masaud, M. M. Milosevic, M. Nedeljkovic, G. Z. Mashanovich, and H. M. H. Chong. Scattering Loss Estimation Using 2-D Fourier Analysis and Modeling of Sidewall Roughness on Optical Waveguides. *IEEE Photonics Journal*, 5(3), June 2013.

[11] C. G. Poulton, C. Koos, M. Fujii, A. Pfrang, T. Schimmel, J. Leuthold, and W. Freude. Radiation Modes and Roughness Loss in High Index-Contrast Waveguides. *IEEE Journal of Selected Topics in Quantum Electronics*, 12(6):1306–1321, November 2006.

[12] T. Horikawa, D. Shimura, and T. Mogami. Low-loss Silicon Wire Waveguides for Optical Integrated Circuits. *MRS Communications*, 6(1):9–15, December 2015.

[13] K.K. Lee, D.R. Lim, H.C. Luan, A. Agarwal, J. Foresi, and L.C. Kimerling. Effect of Size and Roughness On Light Transmission in a Si/SiO2 Waveguide Experiments and Model. *Applied Physics Letters*, 77(11):1617–1619, 2000.

[14] J.P.R. Lacey and F.P. Payne. Radiation Loss From Planar Waveguides With Random Wall Imperfections. *IEE Proceedings*, 137(4):282–288, 1990.

[15] T. Barwicz and H. A. Haus. Three-Dimensional Analysis of Scattering Losses Due to Sidewall Roughness in Microphotonic Waveguides. *Journal of Lightwave Technology*, 23(9):2719–2732, September 2005.

[16] F.P. Payne and J.P.R. Lacey. A Theoretical Analysis of Scattering Loss From Planar Optical Waveguides. *Optical and Quantum Electronics*, 26(10):977–986, 1994.

[17] M. Kuznetsov and H. A. Haus. Radiation Loss in Dielectric Waveguide Structures by the Volume Current Method. *IEEE Journal of Quantum Electronics*, QE-19(10):1505–1514, 1983.

[18] Ata Zadehgol. SHF: SMALL: A Novel Algorithm for Automated Synthesis of Passive, Causal, and Stable Models for Optical Interconnects. National Science Foundation (NSF) Award #1816542. Proposal submitted on 11/15/2017. Grant period: 10/1/2018-9/30/2021.

[19] K. S. Yee. Numerical Solution of Initial Boundary Value Problems Involving Maxwells Equations in Isotropic Media. *IEEE Transactions on Antennas and Propagation*, Ap14(3):302, 1966.

[20] Allen Taflove and Susan C. Hagness. *Computational Electrodynamics: The Finite-Difference Time-Domain Method.* Artech House Inc., Norwood, MA, 3rd edition, 2005.

[21] J. Alan Roden and Stephen D. Gedney. Convolution PML (CPML) An Efficient FDTD Implementation of the CFS – PML for Arbitrary Media. *MICROWAVE AND OPTICAL TECHNOLOGY LETTERS*, 27(5), 2000.

[22] H. Kogelnik. *Theory of Dielectric Waveguides*, pages 13–81. Springer Berlin Heidelberg, Berlin, Heidelberg, 1975.

[23] C. A. Balanis. *Advanced Engineering Electromagnetics.* Wiley, USA, 2nd edition, 2012.

[24] M. C. Gupta and J. Ballato. *The Handbook of Photonics*. CRC Press, Taylor & Francis Group, Boca Raton, 2nd edition, 2018.

[25] F. Ladouceur. Roughness, Inhomogeneity, and Integrated Optics. *Journal of Lightwave Technology*, 15(6):1020–1025, June 1997.

[26] A. D. Simard, N. Ayotte, S. Bédard, and S. LaRochell. Impact of Sidewall Roughness on Integrated Bragg Gratings. *Journal of Lightwave Technology*, 29(24):3693–3704, December 2011.

[27] G. Pandraud, E. Margallo-Balbas, C. K. Yang, and P. J. French. Experimental Characterization of Roughness Induced Scattering Losses in PECVD SiC Waveguides. *Journal of Lightwave Technology*, 29(5):744–749, March 2011.

[28] F. Grillot, L. Vivien, S. Laval, and E. Cassan. Propagation Loss in Single-Mode Ultrasmall Square Silicon-on-Insulator Optical Waveguides. *Journal of Lightwave Technology*, 24(2):891–896, February 2006.

[29] K. P. Yap, A. Delâge, J. Lapointe, B. Lamontagne, J. H. Schmid, P. Waldron, B. A. Syrett, and S. Janz. Correlation of Scattering Loss, Sidewall Roughness and Waveguide Width in Silicon-on-Insulator (SOI) Ridge Waveguides. *Journal of Lightwave Technology*, 27(18):3999–4008, September 2009.

[30] I. Papakonstantinou, R. James, and D. R. Selviah. Radiation- and Bound-Mode Propagation in Rectangular, Multimode Dielectric, Channel Waveguides With Sidewall Roughness. *Journal of Lightwave Technology*, 27(18):4151–4163, September 2009.

[31] S. Bakirtzis, X. Zhang, and C. D. Sarris. Stochastic Modeling of Wave Propagation in Waveguides With Rough Surface Walls. *Transactions on Microwave Theory and Techniques*, 69(1):500–508, January 2021.

[32] Christian Ranacher, Andreas Tortschanoff, Cristina Consani, Nithin Ravi Kumar, Mohssen Moridi, Thomas Grille, and Bernhard Jakoby. Intrinsic Damping in Silicon Slab Waveguides in the Mid-Infrared. In *2017 IEEE Photonics Society Summer Topical Meeting Series (SUM)*, pages 65–66, 2017.

[33] Pyspeckle. `https://pyspeckle2.readthedocs.io/en/latest/#`. Accessed: Oct. 15, 2021.

[34] M. Deserno. How to Generate Exponentially Correlated Gaussian Random Numbers. August 2002.

[35] D. M. Pozar. *Microwave Electronics*. Wiley, USA, 4th edition, 2012.

[36] Brian Guiana. Optical Interconnect Designer Tool (OIDT). `https://github.com/bmguiana/OIDT`. Created on November 23, 2021.

[37] J. W. Brown and R. V. Churchill. *Complex Variables and Applications*. McGraw-Hill, New York, NY, USA, 8th edition, 2009.

[38] Ata Zadehgol. Deterministic Reduced-Order Macromodels for Computing the Broadband Radiation-Field Pattern of Antenna Arrays in FDTD. *IEEE Transactions on Antennas and Propagation*, 64(6):2418–2430, 2016.

[39] James W. Cooley and John W. Tukey. An Algorithm for the Machine Calculation of Complex Fourier Series. *Mathematics of Computation*, 19(90):297–301, 1965.

[40] Dennis M. Sullivan. *Electromagnetic Simulation Using the FDTD Method*. Wiley-IEEE Press, Piscataway, NJ, USA, 2 edition, 2013.

[41] GNU General Public License v3.0. `https://www.gnu.org/licenses/gpl-3.0.en.html`. Accessed: Oct. 20, 2021.